The importance of the pericardium for cardiac biomechanics: From physiology to computational modeling

Martin Pfaller, Julia Hoermann, Martina Weigl, Andreas Nagler, Radomir Chabiniok, Cristóbal Bertoglio, Wolfgang A. Wall

Biomechanics and Modeling in Mechanobiology manuscript No.
(will be inserted by the editor)

The importance of the pericardium for cardiac biomechanics

From physiology to computational modeling

Martin R. Pfaller[1] · Julia M. Hörmann[1] · Martina Weigl[1] · Andreas Nagler[1] · Radomir Chabiniok[2,3,4] · Cristóbal Bertoglio[5*] · Wolfgang A. Wall[1*]

Received: date / Accepted: date

Abstract The human heart is enclosed in the pericardial cavity. The pericardium consists of a layered thin sac and is separated from the myocardium by a thin film of fluid. It provides a fixture in space and frictionless sliding of the myocardium. The influence of the pericardium is essential for predictive mechanical simulations of the heart. However, there is no consensus on physiologically correct and computationally tractable pericardial boundary conditions. Here we propose to model the pericardial influence as a parallel spring and dashpot acting in normal direction to the epicardium. Using a four-chamber geometry, we compare a model with pericardial boundary conditions to a model with fixated apex. The influence of pericardial stiffness is demonstrated in a parametric study. Comparing simulation results to measurements from cine magnetic resonance imaging reveals that adding pericardial boundary conditions yields a better approximation with respect to atrioventricular plane displacement, atrial filling, and overall spatial approximation error. We demonstrate that this simple model of pericardial-myocardial interaction can correctly predict the pumping mechanisms of the heart as previously assessed in clinical studies. Utilizing a pericardial model can not only provide much more realistic cardiac mechanics simulations but also allows new insights into pericardial-myocardial interaction which cannot be assessed in clinical measurements yet.

Keywords Cardiac mechanical modeling · Pericardium · Boundary conditions · Finite element simulation

M. R. Pfaller
martin.pfaller@tum.de

[1]Institute for Computational Mechanics, Technical University of Munich, Boltzmannstr. 15, 85748 Garching b. München, Germany

[2] Inria, Paris-Saclay University, Palaiseau, France

[3] LMS, Ecole Polytechnique, CNRS, Paris-Saclay University, Palaiseau, France

[4] School of Biomedical Engineering & Imaging Sciences (BMEIS), St Thomas' Hospital, King's College London, UK

[5] Bernoulli Institute for Mathematics, Computer Science and Artificial Intelligence, University of Groningen, Nijenborgh 9, 9747 AG Groningen, The Netherlands

∗ joint last authors

1 Introduction

1.1 Motivation

Cardiac mechanics simulations consist of solving a nonlinear elastodynamic boundary value problem [2]. Physiological boundary conditions are essential to achieve predictive results for any clinical purposes. The boundary conditions on the structure field of the myocardium are mainly governed by two physiological aspects: Blood flow within the chambers near the inside surface of the myocardium (*endocardium*) and the pericardial sac on the outside surface (*epicardium*), see figure 1a. There are many applications for simulating heart blood flow [3]. However, for many relevant questions the exact fluid dynamics of blood within the heart or a resolved fluid-solid interaction simulation are often not needed for simulating the myocardium. Instead, a realistic pressure-flow relationship stemming from the circulatory system is sufficient, which is commonly represented by lumped-parameter fluid models that provide the correct normal pressure to the endocardial wall [4].

However, there is no consensus on boundary conditions to represent the effects of the pericardial sac. The

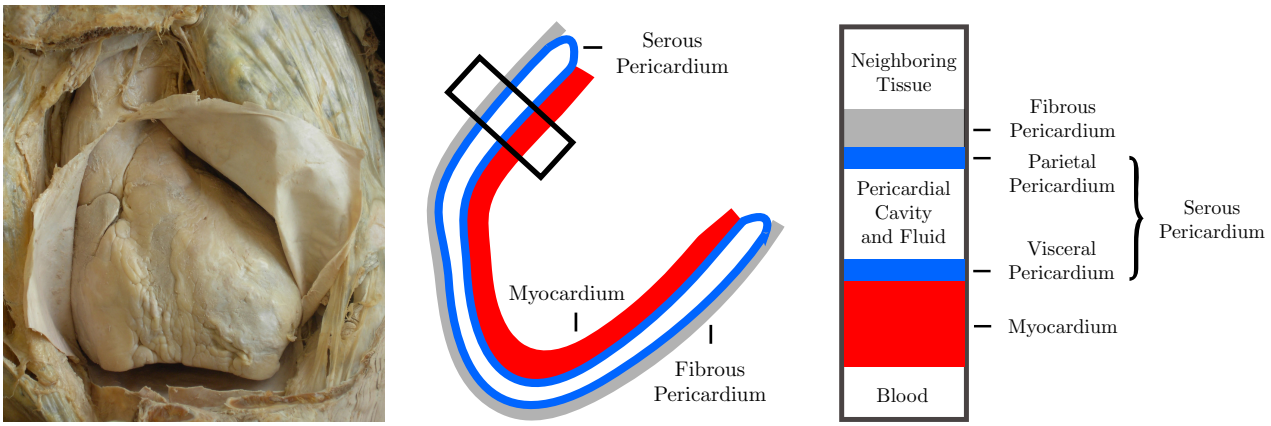

(a) Dissected mediastinum with cut pericardium and heart surface. Image by G. M. Gruber, Medical University of Vienna, Austria.

(b) Location of the heart with respect to serous and fibrous pericardium. Inspired by [1].

(c) Cross-sectional view of transmural layers of heart and pericardium. Inspired by [1].

Fig. 1: Heart and pericardium.

goal of this work is twofold: (a) to provide a detailed literature review of pericardial biomechanics, hence justifying its modeling using a computationally inexpensive viscoelastic model, and (b) to highlight the relevance of such boundary conditions through a detailed quantitative analysis using a subject-specific cine MRI data set. We employ a four-chamber geometry including parts of the great vessels, as it provides us with additional options to asses the physiological correctness of our boundary condition, e.g. through the interplay between ventricles and atria during ventricular systole. Note, however, that the pericardial boundary condition is independent of the geometry and is meant to be applied to any kind of cardiac mechanics simulation that includes the epicardial surface.

This work is structured as follows. Following a review of the anatomy and physiology of the pericardium in section 1.2, we review pericadial boundary conditions currently used in cardiac mechanics simulations. We propose a model to represent the influence of the pericardium by parallel springs and dashpots acting in normal direction to the epicardium in section 2. Furthermore, we summarize a three-dimensional elastodynamical continuum model for the myocardium which is monolithically coupled to a zero-dimensional reduced-order windkessel model for the circulatory system. We demonstrate the influence of the pericardial boundary condition in section 3 through a detailed quantitative comparison of simulation results to cine MRI. For that we evaluate ventricular volume, atrioventricular-plane-displacement, atrioventricular interaction, and introduce a quantitative error measurement by calculating a distance error at endo- and epicardial surfaces between simulation results and cine MRI. We close this work with a discussion of the results, the limitations of our study, future perspectives, and some conclusions in section 4.

1.2 The pericardium

In the following, we review the anatomy of the pericardium and its physiology, where we focus on the mechanical interaction between the pericardium and the heart. Based on this review, we evaluate variants of pericardial boundary conditions and propose a model for pericardial-myocardial interaction.

1.2.1 Anatomy

As shown in figure 1a, the pericardium is a sac-like structure with a combined thickness of 1-2 mm that contains the heart and parts of the great vessels [5]. Figures 1b and 1c show a cross-sectional view of the myocardium and the layers of the pericardium. A common analogy for the location of the heart within the pericardium is that of a fist pushed into an inflated balloon [6].

The *fibrous pericardium* consists of a fibrous layer that forms a flask-like sac with a wavy collagenous structure of three interwoven main layers that are oriented 120° to each other [7]. It has a higher tensile stiffness than the myocardium and is dominated by the viscoelastic behavior of extracellular collagen matrix and elastin fibers [8]. The fibrous pericardium is fixed in space by a "three point cardiac seat belt" via the pericardial ligaments to the sternum. Furthermore, it

is thoroughly attached to the central tendon of the thoracic diaphragm and additionally supported by the coats of the great vessels [9]. The various tissues, the fibrous pericardium is in contact with, can be seen in figure 2.

The fibrous pericardium contains a serous membrane, the *serous pericardium*, forming a closed sac. The serous pericardium is connected to the myocardium (*visceral pericardium*) and the fibrous pericardium (*parietal pericardium*). The composite of fibrous and parietal pericardium is commonly referred to as pericardium, whereas the visceral pericardium in contact with the myocardium is referred to as epicardium [9]. The space between the visceral and parietal pericardium is the pericardial cavity, which is filled by a thin film of fluid with an average volume of 20-25 ml [5]. Beneath the visceral pericardium the heart is covered by a layer of adipose tissue, accumulated especially in the interventricular and atrioventricular grooves and around the coronary vessels, constituting about 20% of the heart weight [10].

1.2.2 Mechanical physiology

The pericardium serves multiple purposes [11] that can be grouped in: (a) membranous, it serves as a barrier against the spread of infection [7] and (b) mechanical, it secures cardiac stability via its attachments within the thorax [12], as will be explained in the following. The mechanical properties of the pericardium itself can be found in [13].

There is clear empirical evidence that the pericardium has a direct mechanical impact on the acute and chronic biomechanics of the heart. For example, in [14] it was discovered that the correlation of left and right ventricular pressure is higher with intact pericardium than after its complete removal. Maximal cardiac output during exercise can be increased acutely by the complete removal of the pericardium (*pericardiectomy*) through utilizing the Frank-Starling mechanism [15]. However, removing the pericardial restraint chronically promotes eccentric hypertrophy, i.e. an increase in dimension and mass of the heart and a change in shape from elliptical to spherical. The pericardium thus acts as a diastolic constraint for the heart by exercising a radial compression stress. This was confirmed in [16] where it was observed that the opening angle of the myocardium with intact visceral pericardium is much higher than after its removal. The visceral pericardium is thus important for residual stress and passive stiffness.

It is widely accepted that the mechanism of the myocardium-pericardium interaction is through the pericardial fluid. In [17] it was found that while increasing the volume of fluid within the pericardial cavity, the pericardial liquid pressure remains constant until it suddenly rises sharply. This led to the conclusion that most of the fluid is contained in pericardial sinuses and groves. This mostly empty space forms the so-called pericardial reserve volume, acting as a buffer against increasing pericardial liquid pressure. Only a small portion of the pericardial fluid remains as a thin film on the interface between parietal and visceral pericardium. In [18], a dye was injected into the pericardial cavity near the apex. Fifteen minutes after injection the dye was almost exclusively found in the interventricular and atrioventricular grooves. This suggests that there is no significant fluid movement on the large surface areas of the ventricular free walls, leaving just a very thin film of fluid with an estimated thickness of less than 0.5 mm.

The mechanical constraint of the pericardium on diastolic cardiac function can be quantified by pericardial pressure. Here it is important to distinguish between liquid pressure and contact pressure [19,20]. Liquid pressure describes the hydrostatic pressure inside the pericardial fluid and is measured by an open-ended catheter. However, liquid pressure does not describe the constraining effect of the pericardium on the myocardium. The constraint is assessed by contact pressure, which can be measured by a thin, flat, air-filled balloon catheter. In [19] it was found that liquid pressure is substantially below contact pressure unless the pericardium contains a significant amount of pericardial fluid, which happens e.g. due to pericardial effusion. Furthermore, contact stress and thus ventricular restraint was maintained even though pericardial fluid was completely removed and liquid pressure at the epicardial surface was zero. Pericardial fluid therefore acts as lubrication rather than a load balancing mechanism, providing low-friction sliding between pericardium and epicardium [21].

There is less information available on the influence of the pericardium during systole. A pericardial restraining effect during systole would require a tension force to be transmitted by the myocardial-pericardial interface. The restraining effect of the pericardium during systole can be well observed in fish, where the parietal pericardium is almost rigid [5]. It was observed in [22] that pericardial liquid pressure in smooth dogfish is always negative and decreases further during cardiac contraction. In man, [23] found that pericardial liquid pressure also drops during ventricular systole but remains positive throughout the cardiac cycle. However, to the best of the authors' knowledge there is no study on the change of contact pressure during systole. It can be observed from mammal cine MRI that surrounding tissue moves toward the heart during systole, indi-

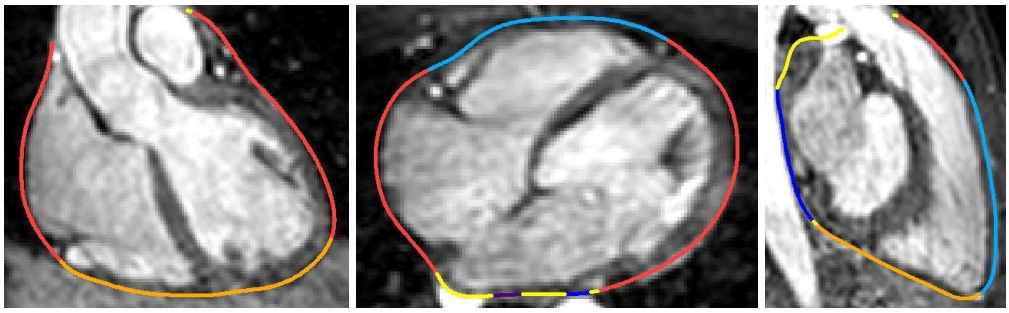

(a) Coronal plane (b) Transverse plane (c) Sagittal plane

Fig. 2: Position of the pericardium indicated in 3D MRI taken during diastasis. The neighboring tissue is color-coded: lungs (red), diaphragm (orange), sternum and ribs (light blue), aorta (dark blue), esophagus (purple), other (yellow). MRI courtesy of R. Chabiniok, J. Harmer, E. Sammut, King's College London, UK.

cating attachment of pericardium and epicardium. We hypothesize that during systole, through the effect of adhesion, the pericardium remains in contact with the epicardium. This is analogous to the simple experiment of "gluing" two glass plates together with a drop of water. The glass plates can hardly be separated in normal direction but can be easily moved relatively to each other in tangential direction.

1.2.3 Current pericardial boundary conditions

For biventricular geometries, the constraining effect of the pericardium in diastole is accounted for in [24,25,26], where a no penetration condition is enforced on the epicardium by a unidirectional penalty contact with a rigid pericardial reference surface. However, this neglects any constraining in systole by not allowing the pericardial interface to transmit any tension forces. Recently, it was proposed in [27] to completely prohibit movement normal to the epicardial surface, neglecting any elastic effects. The bi-directional elastic constraining effect of the pericardium is accounted for in spring-type boundary conditions, where a spring-dashpot boundary condition is enforced either on the base [2] or on apex and valve annuli [28] with homogeneous Neumann conditions applied to the rest of the epicardium. These boundary conditions are analogous to the external tissue support of the aorta in [29,30]. However, they do not cover the whole epicardial surface thus representing pericardial-myocardial interaction only partially.

Fewer references exist for four chamber geometries. A common combination of boundary conditions for four chamber geometries are homogeneous Dirichlet conditions on vessel cut-offs and a soft material connected to the apex [25,31], or springs on the outside of great vessels [32]. In those cases, however, homogeneous Neumann conditions are applied on the remaining epicardial surface, neglecting any influence of the pericardium as in the biventricular case. In [33] "omni-directional" springs acting in all directions are applied to the epicardium, artificially constraining any sliding movement along the pericardial-epicardial interface. To the authors' best knowledge, the most detailed and physiologically correct representation of the pericardium so far was implemented in [34]. The pericardial-myocardial interaction was here modeled by a frictionless sliding, bi-directional penalty contact interaction in normal direction between the epicardium and a solid pericardial reference body. However, this condition is computationally very expensive as it requires solving an adhesial contact interaction problem. It also requires an additional solid body to be created, representing the surrounding tissue. Furthermore, no boundary conditions could be enforced at the great vessels since they were not included in the geometry. Thus, a fixation of the apex was necessary. All models based on four chamber geometries reviewed here lack a quantitative validation through comparison of simulation results to measurements, e.g. medical images like magnetic resonance imaging (MRI).

2 Models

In this work, we use a patient-specific four-chamber geometry from high-resolution static 3D MRI, including ventricles, atria, adipose tissue, and great vessels. Our cardiac model is formulated in a large displacement, constitutive nonlinear framework with nonlinear boundary conditions. It features high-resolution quadratic tetrahedral finite elements for structural dynamics with implicit time integration. Blood pressure is incorporated through monolithic coupling of the left and right ventricle to windkessel models which include each the atrioventricular and semilunar valves. The reference con-

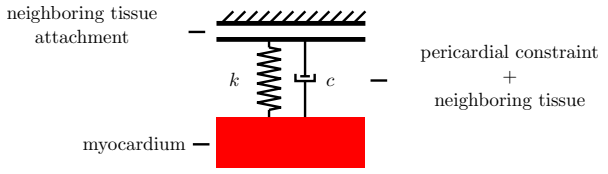

Fig. 3: Serous pericardium, fibrous pericardium, and neighbouring tissue modeled by a spring (stiffness k) and a dashpot (viscosity c) in parallel. Spring and dashpot act in normal direction of the epicardial surface.

figuration is prestressed in all four cardiac chambers. The passive myocardial material features a state of the art orthotropic exponential material law proposed in [35]. Myofiber contraction in atria and ventricles is modeled with an active stress approach. Passive and active material behavior is based on local fiber orientations.

We follow the classic approach of nonlinear large deformation continuum mechanics to model the elastodynamic problem of 3D cardiac contraction. We define the reference configuration $\boldsymbol{X}$ and current configuration $\boldsymbol{x}$ which are connected by the displacements $\boldsymbol{u} = \boldsymbol{x} - \boldsymbol{X}$. We calculate the deformation gradient $\boldsymbol{F}$, the Green-Lagrange strain tensor $\boldsymbol{E}$, and the right Cauchy-Green tensor $\boldsymbol{C}$

$$\boldsymbol{F} = \frac{\partial \boldsymbol{x}}{\partial \boldsymbol{X}}, \quad \boldsymbol{E} = \frac{1}{2}(\boldsymbol{C} - \boldsymbol{I}), \quad \boldsymbol{C} = \boldsymbol{F}^{\mathrm{T}}\boldsymbol{F}. \tag{1}$$

2.1 Modeling the pericardium

Our aim in this work is to propose and justify a pericardial boundary condition that is both realistic and computationally inexpensive. The pericardial model we propose is based on [36] and is sketched in figure 3. Using our code it was also already applied to a two-chamber geometry in [37]. It consists of a spring and a dashpot in parallel acting in normal direction to the epicardial surface. Within the tangential plane we allow frictionless sliding to account for the lubricating effect of the pericardial fluid. A spring stiffness k and dashpot viscosity c contain the combined effects of serous pericardium, fibrous pericardium, and neighboring tissue. Generalizing the effect on the ventricles, spring compression models the pericadium's constraining effect during passive ventricular filling, whereas spring expansion models the pericadium's support during ventricular systole.

Note that only in the limit case of $k \to \infty$, we would obtain a boundary condition that penalizes and therefore prohibits any movement in normal direction to the epicardium, as it was recently proposed in [27]. However, our pericardial boundary condition is meant to be used with finite values for k and v, more realistically representing the visco-elastic support of the pericardium and its surrounding tissue and permitting movement normal to the epicardial surface. Furthermore, our parametric study in section 3.2 shows that small values of k lead to physiological results.

In the following, we will derive a simple mathematical formulation for the pericardial boundary condition depicted in figure 3. This derivation will be carried out in two steps, where different assumptions are introduced in each step. Only the spring component will be considered during the derivation. However, all conclusions hold equivalently for the dashpot component.

Our goal is to preserve the features of the detailed pericardial boundary condition in [34] but arrive at a much simpler and cheaper formulation. As reviewed in section 1.2.3, pericardial-myocardial interaction is modeled in [34] by adhesial contact between the epicardium and an elastic reference body that is fixed in space and representing the surrounding tissue, see figure 4a.

In the first step, we replace the elastic body representing the surrounding tissue in [34] with springs acting in normal direction to the epicardium. Here, we assume that the elasticity of the surrounding tissue is linear with respect to the small movements of the epicardium in its normal direction. Note that we enforce the boundary conditions on the epicardial side of the myocardial-pericardial interface, as this does not require a representation of the actual pericardial surface. We therefore do not model the pericardium itself but the forces acting on the myocardium because of its presence. The elastic potential of a linear spring distributed on the epicardial surface Γ^{epi} in current configuration surface is

$$W = \frac{1}{2}\int_{\Gamma^{\mathrm{epi}}} k g^2 \, \mathrm{d}a \tag{2}$$

with spring stiffness k, gap g, and surface integral in current configuration $\mathrm{d}a$. The calculation of the gap is illustrated in figure 4b. We project a point $\boldsymbol{x} \in \Gamma^{\mathrm{epi}}$ on the current epicardial surface onto the point $\boldsymbol{X}_{\mathrm{proj}} \in \Gamma_0^{\mathrm{epi}}$ on the reference epicardial surface. The distance between both points projected in the direction of the current outward normal vector $\boldsymbol{n}$ yields the gap function

$$g = (\boldsymbol{x} - \boldsymbol{X}_{\mathrm{proj}}) \cdot \boldsymbol{n}. \tag{3}$$

Though reducing algorithmic and computational demands compared to contact interaction, this boundary condition still requires updates of the normal vector and its linearization with respect to the displacements as well as a projection of each evaluation point onto Γ_0^{epi} in each Newton iteration at each time step.

In a second step, we introduce two further simplifications. Instead of calculating the spring deformation

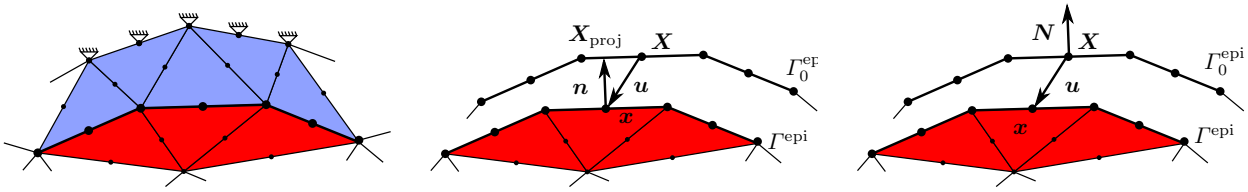

(a) Adhesial contact interaction from [34] between myocardium and fixed surrounding tissue (blue).

(b) Current normal spring from (3).

(c) Reference normal spring from (4).

Fig. 4: Different formulations of interaction between myocardium (red) and pericardium.

from a projection, we directly use the spatial displacements $\boldsymbol{u}$. Furthermore, we use the epicardial normal vector in reference configuration (i.e. $\boldsymbol{N}$ instead of $\boldsymbol{n}$), neglecting any change in normal direction throughout the simulation. The formulation of the gap in (3) is then simplified to

$$g = \boldsymbol{u} \cdot \boldsymbol{N} \tag{4}$$

The simplifications leading to (4) are valid for small rotations of the epicardium, an assumption that is not valid for all parts of the epicardium. However, the performance of both formulations (3) and (4) is reviewed in appendix A.

We then arrive at the final expression for the pericardial boundary traction $\boldsymbol{t}_{epi}$ acting on the epicardial surface

$$\boldsymbol{t}_{epi} = \boldsymbol{N} \left(k_p \boldsymbol{u} \cdot \boldsymbol{N} + c_p \dot{\boldsymbol{u}} \cdot \boldsymbol{N} \right) . \tag{5}$$

For the sake of simplicity, we use here constant boundary condition parameters k_p and c_p on the whole epicardial surface. As it will be shown in the numerical examples, this simple approach already leads do greatly improved results. But of course, a regional distribution based on neighboring organs as visualized in figure 2 is also possible.

2.2 Geometrical model

To illustrate the effects of our pericardial model, we employ a four chamber geometry obtained in vivo from a 33 year old healthy female volunteer. The imaging data was acquired at King's College London, UK using a Philips Achieva 1.5T magnetic resonance imaging (MRI) scanner with a dual-phase whole-heart 3D b-SSFP sequence [38], acquisition matrix $212 \times 209 \times 200$, acquired voxel size $2 \times 2 \times 2$ mm, repetition time 4.5 ms, echo time 2.2 ms, echo train length 26 and flip angle 90°. The diastolic rest period (diastasis) was used to generate the computational mesh. The geometry was meshed using Gmsh [39] with a resolution of 2 mm, yielding 282 288 nodes and 167 232 quadratic tetrahedral elements, totalling a 846 864 structural degrees of freedom. Additionally, our geometry contains triangular surface elements with no additional degrees of freedom to track the movement of the planes of cardiac valves, allowing us to monitor the volumes of all four cardiac cavities. All four cardiac cavities are closed with surface elements with no additional degrees of freedom at the valve planes depicted in red in figure 5c at the left and right atrioventricular plane, respectively. The atria are additionally closed at their respective connections to the vasculature. We can thus monitor the volumes of all four cardiac cavities and track the movement of cardiac valve planes. The meshed geometry is shown in figure 5a. The different materials are depicted in figure 5c.

Additionally, we prescribe the local angles of cardiac myofibers at epi- and endocardium of the ventricles. Using harmonic lifting, the fiber vectors $\boldsymbol{f}_0$ are interpolated to the interior of the domain by solving a Laplace problem [40]. We interpolate the fiber orientation smoothly at each integration point. It is well known that the fiber orientation has a strong impact on passive and active cardiac mechanics [41,42,43,44,45,46]. In order to make a more clear statement about the pericardial boundary conditions independently of the fiber orientation and to show the interplay between boundary conditions and fiber orientations, we compare in this work three different fiber distributions: ±50°, ±60°, and ±70°. The first and second angle describe the fiber helix angle at the endo- and epicardial surface, respectively, with respect to the local circumferential axis. The transverse angle is zero throughout the myocardium. The sheet normal vector $\boldsymbol{n}_0$ is perpendicular to the epi- and endocardial surfaces. The sheet vector $\boldsymbol{s}_0$ is then obtained from $\boldsymbol{s}_0 = \boldsymbol{n}_0 \times \boldsymbol{f}_0$. The atrial fiber architecture is obtained using a semi-automatic registration method based on the fiber definition in atlas atria [47,48]. See figure 5b for atrial fibers and ventricular ±60° fibers visualized at the endocardium.

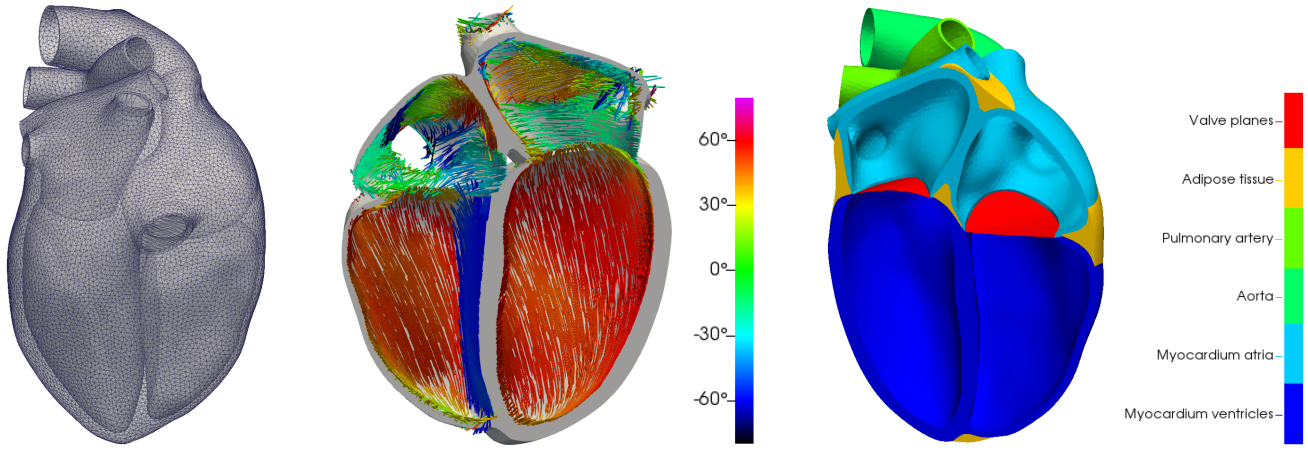

(a) Computational mesh.

(b) Atrial fibers and ventricular ±60° fibers at endocardium. Color shows helix angle with respect to long axis.

(c) Materials.

Fig. 5: Four chamber patient-specific cardiac geometry.

2.3 Modeling cardiac contraction

Balance of momentum, a Neumann windkessel coupling condition with left ventricular pressure p_v acting on the left endocardium Γ_0^{endo}, omni-directional spring-dashpot boundary conditions, and pericardial boundary conditions yield the energy $\delta\Pi$ of the boundary value problem

$$\begin{aligned}\delta\Pi = &\int_{\Omega_0} \rho_0\, \ddot{\boldsymbol{u}} \cdot \delta\boldsymbol{u}\, \mathrm{d}V + \int_{\Omega_0} \boldsymbol{S} : \delta\boldsymbol{E}\, \mathrm{d}V \\ &+ \sum_{\nu\in\{l,r\}} \int_{\Gamma_0^{\text{endo},\nu}} p_v^{\nu}\, \boldsymbol{F}^{-\mathrm{T}} \cdot \boldsymbol{N} \cdot \delta\boldsymbol{u}\, \mathrm{d}A \\ &+ \int_{\Gamma^{\text{vess}}} [k_v \boldsymbol{u} + c_v \dot{\boldsymbol{u}}] \cdot \delta\boldsymbol{u}\, \mathrm{d}A\end{aligned} \tag{6}$$

with density ρ_0, accelerations $\ddot{\boldsymbol{u}}$, the second Piola-Kirchhoff stress tensor $\boldsymbol{S}$, and spring stiffnesses k_v, k_a and viscosities c_v, c_a for vessel and apical surfaces Γ^{vess} and Γ^{apex}, respectively. Furthermore, we have virtual displacements $\delta\boldsymbol{u}$ and virtual strains $\delta\boldsymbol{E}$. Omni-directional springs and dashpots are placed on the outsides of the great vessels Γ^{vess} and apical surface Γ^{apex}. The energy $\delta\Pi$ is complemented in section 3 by the energy of different boundary conditions.

We define different materials with the volumes defined as in figure 5 for adipose tissue (7), ventricular and atrial myocardium (8), and aorta and pulmonary artery (9):

$$\boldsymbol{S} = \frac{\partial}{\partial \boldsymbol{E}} \left(\psi_{\text{NH}} + \psi_{\text{vol}}\right) + \frac{\partial}{\partial \dot{\boldsymbol{E}}}\, \psi_{\text{visco}}, \tag{7}$$

$$\boldsymbol{S} = \frac{\partial}{\partial \boldsymbol{E}} \left(\psi_{\text{exp}} + \psi_{\text{vol}}\right) + \frac{\partial}{\partial \dot{\boldsymbol{E}}}\, \psi_{\text{visco}} + \boldsymbol{S}_{\text{act}}, \tag{8}$$

$$\boldsymbol{S} = \frac{\partial}{\partial \boldsymbol{E}} \left(\psi_{\text{MR}} + \psi_{\text{vol}}\right) + \frac{\partial}{\partial \dot{\boldsymbol{E}}}\, \psi_{\text{visco}}. \tag{9}$$

Each material is composed of a hyperelastic and a viscous contribution depending on the rate of Green-Lagrange strains $\dot{\boldsymbol{E}}$. The viscous behavior of myocardial tissue is modeled with a viscous pseudo-potential. Only the ventricular tissue in (8) has an additional active stress component $\boldsymbol{S}_{\text{act}}$. The strain energy density functions for exponential orthotropic solid ψ_{exp} [35], Mooney-Rivlin solid [2,25] ψ_{MR}, Neo-Hookean solid ψ_{NH}, penalty function ψ_{vol}, and viscous pseudo-potential [49] ψ_{visco} are given as

$$\begin{aligned}\psi_{\text{exp}} = &\frac{a}{2b}\left(e^{b(\bar{I}_1-3)} - 1\right) + \frac{a_{fs}}{2b_{fs}}\left(e^{b_{fs} I_{8,fs}^2} - 1\right) \\ &+ \sum_{i\in\{f,s\}} \frac{a_i}{2b_i}\left(e^{b_i (I_{4,i}-3)} - 1\right), \\ \psi_{\text{MR}} = C_1(\bar{I}_1 - 3) + C_2(\bar{I}_2 - 3), &\quad \psi_{\text{NH}} = \frac{\mu}{2}(\bar{I}_1 - 3), \\ \psi_{\text{vol}} = \frac{\kappa}{2}\left(1 - J\right)^2, &\quad \psi_{\text{visco}} = \frac{\eta}{2}\mathrm{tr}\left(\dot{\boldsymbol{E}}^2\right),\end{aligned} \tag{10}$$

with the Jacobian $J = \det \boldsymbol{F}$ of the deformation gradient and material parameters a_i, b_i, μ, C_1, and C_2,

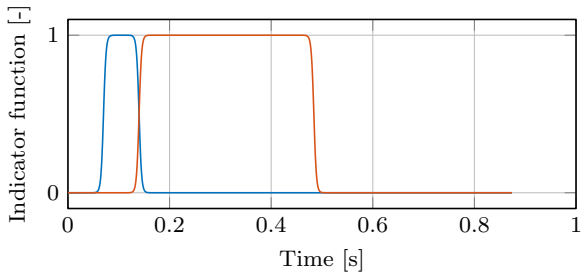

(a) Prescribed indicator functions $f(t)$ for atria (blue) and ventricles (red).

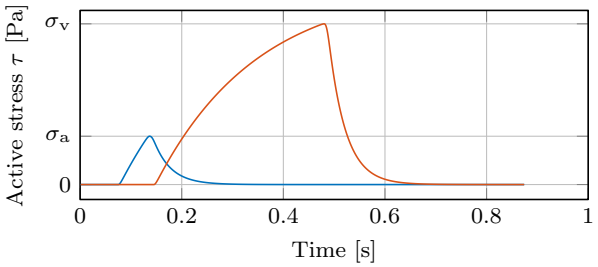

(b) Active stress $\tau(t)$ for atria (blue) and ventricles (red) with maximum values σ_a and σ_v, respectively.

Fig. 6: Active stress.

penalty parameter κ, viscosity η, and invariants

$$\begin{aligned} &\bar{I}_1 = J^{-2/3} I_1, \quad \bar{I}_2 = J^{-4/3} I_2, \\ &I_1 = \operatorname{tr} \boldsymbol{C}, \quad I_2 = \frac{1}{2}\left[\operatorname{tr}^2(\boldsymbol{C}) - \operatorname{tr}\left(\boldsymbol{C}^2\right)\right], \\ &I_{4,f} = \boldsymbol{f}_0 \cdot \boldsymbol{C}\boldsymbol{f}_0, \quad I_{4,s} = \boldsymbol{s}_0 \cdot \boldsymbol{C}\boldsymbol{s}_0, \quad I_{8,fs} = \boldsymbol{f}_0 \cdot \boldsymbol{C}\boldsymbol{s}_0. \end{aligned} \tag{11}$$

We use the same active stress approach for both atrial and ventricular myocardium, though with different parameters. However, for simplicity of notation, we do not distinguish between atria or ventricles in the following equations. The active stress is computed as

$$\boldsymbol{S}_{\text{act}} = \tau(t) \cdot \boldsymbol{f}_0 \otimes \boldsymbol{f}_0 \tag{12}$$

with fiber stress τ in local reference fiber direction $\boldsymbol{f}_0$. Based on [50], we model fiber stress by the evolution equation

$$\dot{\tau}(t) = -|a(t)|\tau(t) + \sigma_0 |a(t)|_+ \tag{13}$$

with activation function a, contractility σ_0, and the function $|a(t)|_+ = \max(a(t); 0)$. The activation function $a(t)$ is modeled by

$$a(t) = \alpha_{\max} \cdot f(t) + \alpha_{\min} \cdot [1 - f(t)] \tag{14}$$

with maximum and minimum activation rates $\alpha_{\max}$ and $\alpha_{\min}$, respectively, and functions

$$f(t) = S^+(t - t_{\text{sys}}) \cdot S^-(t - t_{\text{dias}}), \tag{15}$$

$$S^{\pm}(\Delta t) = \frac{1}{2}\left[1 \pm \tanh\left(\frac{\Delta t}{\gamma}\right)\right] \tag{16}$$

with steepness $\gamma = 0.005$ s and descending and ascending sigmoid functions S^+ and S^-, respectively. The indicator function $f \in \,]0, 1[$ indicates systole. The times t_{sys} and t_{dias} model the onset of systole and diastole, respectively. Note that the active stress tensor $\boldsymbol{S}_{\text{act}}$ is the only input of our solid model we prescribe over time. Our structural model can be coupled to a model of electric signal propagation as shown in [51]. However, as the focus in this work is on pericardial boundary conditions, a coupled electro-mechanical model would only introduce unnecessary complexity and variability. Using the parameters in table 1a, we obtain the active stress curve depicted in figure 6b. The values σ_a and σ_v denote the maximum of the active stress τ for atria and ventricles, respectively.

Using the finite element method, we discretize displacements $\boldsymbol{u}$ and virtual displacements $\delta\boldsymbol{u}$ arising in the weak form (6) by

$$\begin{aligned} \boldsymbol{u}^{(e)} &= \boldsymbol{\varphi}^{(e)}(\boldsymbol{X})\ \mathbf{d}^{(e)} \\ \delta\boldsymbol{u}^{(e)} &= \boldsymbol{\varphi}^{(e)}(\boldsymbol{X})\ \delta\mathbf{d}^{(e)} \end{aligned} \tag{17}$$

with quadratic basis functions $\boldsymbol{\varphi}$ and nodal displacements $\mathbf{d}$ on each tetrahedral element (e). Assembly of the discretized problem leads to the matrix notation

$$\mathbf{M}\ddot{\mathbf{d}} + \mathbf{F}(\mathbf{d}, \dot{\mathbf{d}}, p_v) = \mathbf{0}, \tag{18}$$

with mass matrix $\mathbf{M}$, force vector $\mathbf{F}$, and discrete displacements, velocities, and accelerations $\mathbf{d}, \dot{\mathbf{d}}$, and $\ddot{\mathbf{d}}$, respectively. We discretize the boundary value problem in time with Newmark's method [52]

$$\begin{aligned} \dot{\mathbf{d}}_{n+1} &= \frac{\gamma}{\beta\Delta t}(\mathbf{d}_{n+1} - \mathbf{d}_n) - \frac{\gamma - \beta}{\beta}\dot{\mathbf{d}}_n - \frac{\gamma - 2\beta}{2\beta}\Delta t\ddot{\mathbf{d}}_n, \\ \ddot{\mathbf{d}}_{n+1} &= \frac{1}{\beta\Delta t^2}(\mathbf{d}_{n+1} - \mathbf{d}_n) - \frac{1}{\beta\Delta t}\dot{\mathbf{d}}_n - \frac{1 - 2\beta}{2\beta}\ddot{\mathbf{d}}_n, \end{aligned} \tag{19}$$

with parameters $\gamma \in [0, 1]$ and $\beta \in [0, 0.5]$, and time step size $\Delta t = t_{n+1} - t_n$. Additionally, we apply the generalized-α method [53], yielding quantities at a generalized time step $n + 1 - \alpha_i$

$$\begin{aligned} (\bullet)_{n+1-\alpha_i} &= (1 - \alpha_i)(\bullet)_{n+1} + \alpha_i(\bullet)_n, \\ &\alpha_i \in [0, 1], \quad i \in \{f, m\} \end{aligned} \tag{20}$$

depending on the weights α_f and α_m for force vector and mass matrix respectively. Newmark's method in

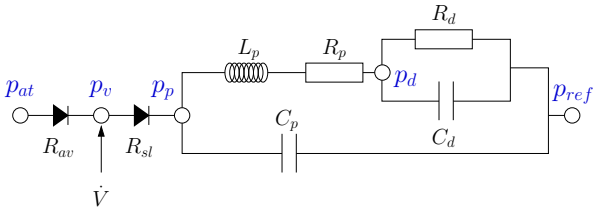

(a) Schematic.

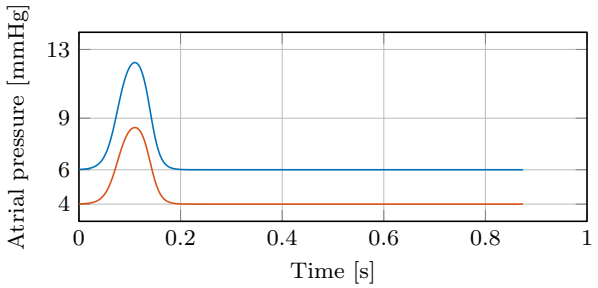

(b) Prescribed left (blue) and right (red) atrial pressure $p_{at}(t)$.

Fig. 7: Windkessel model.

combination with the generalized α-scheme is a common technique for implicit one-step time integration for finite elements in nonlinear solid dynamics. Finally, we obtain the time and space discrete structural residual

$$\mathbf{R}^{\mathrm{S}} = \mathbf{M}\ddot{\mathbf{d}}_{n+1-\alpha_m} + \mathbf{F}_{n+1-\alpha_f}. \tag{21}$$

All parameters used for the elastodynamical model are summarized in table 1a.

2.4 Modeling the circulatory system

We use the same windkessel model for each ventricle with different parameters. For simplicity of notation, we drop in this section the index of the ventricle ν in all windkessel parameters and variables. Note that this cardiovascular model does not represent a closed-loop system since the total blood volume is not conserved, i.e. blood exiting the right ventricle into the lungs does not enter the left atrium. However, using a windkessel model for each ventricle provides us with a reasonable approximation of ventricular pressures.

In this work we use a four element windkessel model based on the ideas in [54] and [4]. A comprehensive review of different windkessel models is given in [55]. The schematic of our windkessel model is given in figure 7a using resistances R, compliances C, and an inertance L_p. Pressures at different parts of the model are denoted by p. We distinguish between a proximal (index p) and a distal part (index d) of the outlets, i.e. lung and aorta for the right and left ventricle, respectively. The atrial pressure p_{at} is prescribed to simulate atrial systole, see figure 7b. The reference pressure p_{ref} is kept constant.

We model the atrioventricular and semilunar valves with a smooth diode-like behavior by non-linear resistances $R_{av} := R(p_v - p_{at})$ and $R_{sl} := R(p_p - p_v)$, respectively, depending on the sigmoid function

$$R(\Delta p) = R_{\min} + (R_{\max} - R_{\min}) \cdot S^{+}(\Delta p) \tag{22}$$

with the steepness k_p of the sigmoid function S^{+} and the minimal and maximal valve resistance $R_{\min} \to 0$ and $R_{\max} \to \infty$, respectively. This yields the set of differential equations

$$\begin{aligned} \frac{p_v - p_{at}}{R_{av}} + \frac{p_v - p_p}{R_{sl}} + \dot{V}(\boldsymbol{u}) &= 0, \\ q_p - \frac{p_v - p_p}{R_{sl}} + C_p \dot{p}_p &= 0, \\ q_p + \frac{p_d - p_p}{R_p} + \frac{L_p}{R_p}\dot{q}_p &= 0, \\ \frac{p_d - p_{\mathrm{ref}}}{R_d} - q_p + C_d \dot{p}_d &= 0. \end{aligned} \tag{23}$$

The 0D windkessel model is strongly coupled to the 3D structural model. The 0D model depends on the structural displacements $\boldsymbol{u}$ of the 3D model via the change in ventricular volume $\dot{V}$. On the other hand, the 3D model depends on left and right ventricular pressure from the 0D model. The coupling between both models is described in section 2.6. The vector of primary variables yields $\mathbf{p} = [p_v, p_p, p_d, q_p]^{\mathrm{T}}$, including the flux q_p through the inertance L_p. We discretize the set of windkessel equations (23) in time with the one-step-θ scheme

$$\begin{aligned} (\dot{\bullet})_{n+1} &= \frac{(\bullet)_{n+1} - (\bullet)_n}{\Delta t}, \quad \theta \in [0,1], \\ (\bullet)_{n+\theta} &= \theta(\bullet)_{n+1} + (1-\theta)(\bullet)_n. \end{aligned} \tag{24}$$

This yields the discrete windkessel residual $\mathbf{R}^{\mathrm{0D}}$ evaluated at time step $n + \theta$. The parameters and initial conditions of the cardiovascular model are summarized in table 1b and table 1c respectively. Windkessel parameters are motivated by values from literature and adapted for this heart to yield physiological pressures as well as approximately a periodic state of the windkessel systems.

2.5 Prestress

For our reference configuration we use a patient-specific geometry segmented from static 3D MRI at diastolic rest period (diastasis), see section 2.2. Diastasis is very

Name	Par.	Value	Unit
All tissues			
Tissue density	ρ_0	10^3	$\left[\frac{\text{kg}}{\text{m}^3}\right]$
Viscosity	η	0.1	[kPa · s]
Volumetric penalty	κ	10^3	[kPa]
Active myocardial tissue			
Atrial contractility	σ_a	9.72	kPa
Ventricular contractility	σ_v	see table 2b	
Activation rate	α_max	+5	$\left[\frac{1}{\text{s}}\right]$
Deactivation rate	α_min	−30	$\left[\frac{1}{\text{s}}\right]$
Atrial systole	t_sys	70	[ms]
Atrial diastole	t_dias	140	[ms]
Ventricular systole	t_sys	see table 2b	
Ventricular diastole	t_dias	484	[ms]
Passive myocardial tissue ([35] table 1, shear, figure 7)			
Matrix	a	0.059	[kPa]
	b	8.023	[−]
Fiber	a_f	18.472	[kPa]
	b_f	16.026	[−]
Sheet	a_s	2.481	[kPa]
	b_s	11.120	[−]
Fiber-sheet	a_{fs}	0.216	[kPa]
	b_{fs}	11.436	[−]
Great vessels			
Mooney-Rivlin	C_1	5.0	[kPa]
Mooney-Rivlin	C_2	0.04	[kPa]
Spring stiffness	k_v	$2.0 \cdot 10^3$	$\left[\frac{\text{kPa}}{\text{mm}}\right]$
Dashpot viscosity	c_v	$1.0 \cdot 10^{-2}$	$\left[\frac{\text{kPa}\cdot\text{s}}{\text{mm}}\right]$
Adipose tissue			
Neo-Hooke	μ	1.0	[kPa]
Pericardial boundary condition			
see table 2a			

(a) Parameters of the elastodynamical model.

Name	Par.	Value	Unit
Proximal inertance	L_p	$1.3 \cdot 10^5$	$\left[\frac{\text{kg}}{\text{m}^4}\right]$
Proximal capacity	C_p	$7.7 \cdot 10^{-9}$	$\left[\frac{\text{m}^4\cdot\text{s}^2}{\text{kg}}\right]$
Distal capacity	C_d	$8.7 \cdot 10^{-9}$	$\left[\frac{\text{m}^4\cdot\text{s}^2}{\text{kg}}\right]$
Proximal resistance	R_p	$7.3 \cdot 10^6$	$\left[\frac{\text{kg}}{\text{m}^4\cdot\text{s}}\right]$
Distal resistance	R_d	$1.0 \cdot 10^8$	$\left[\frac{\text{kg}}{\text{m}^4\cdot\text{s}}\right]$
Reference pressure	p_ref	0	[Pa]
Closed valve resistance	R_max	$1.0 \cdot 10^{13}$	$\left[\frac{\text{kg}}{\text{m}^4\cdot\text{s}}\right]$
Open valve resistance	R_min	$1.0 \cdot 10^6$	$\left[\frac{\text{kg}}{\text{m}^4\cdot\text{s}}\right]$
Valve steepness	k_p	$1.0 \cdot 10^{-3}$	[Pa]

(b) Parameters of the reduced order cardiovascular model (identical for left and right ventricle).

Name	Par.	Value Left	Value Right	Unit
Atrial pressure	$p_{at}(0)$	6.0	4.0	[mmHg]
Ventricular pressure	$p_v(0)$	8.0	6.0	[mmHg]
Proximal pressure	$p_p(0)$	61.8	24.0	[mmHg]
Distal pressure	$p_d(0)$	59.7	23.2	[mmHg]
Proximal flow	$q_p(0)$	38.3	14.9	$\left[\frac{\text{cm}^3}{\text{s}}\right]$

(c) Initial conditions of the reduced order cardiovascular model.

Par.	Value
Generalized-α	
γ, α_f, α_m	0.5
β	0.25
One-step-θ	
θ	1.0

(d) Numerical time integration parameters.

Table 1: Overview of parameters in four-chamber cardiac model.

suitable for the reference configuration, since both ventricular and atrial myofibers are relaxed, the heart is not accelerated, and blood pressures are minimal and constant. This simplifies the task of obtaining the stress state of the reference configuration, which in this case is determined by the static blood pressures within the cardiac cavities. We therefore have to prestress our geometry with the initial ventricular pressure from table 1c. In this work, we use the Modified Updated Lagrangian Formulation as proposed in [56,57]. This method incrementally calculates a deformation gradient with respect to an unknown stress-free reference configuration. From this deformation gradient, a stress field is calculated so that the segmented geometry of the heart is in balance with the prestressed pressure state. This yields a prestress within the myocardium as well as in the pericardial boundary condition in case *pericardium*. Note that while this technique allows to model prestress, we do not account for the residual stress inherent in myocardial tissue [16].

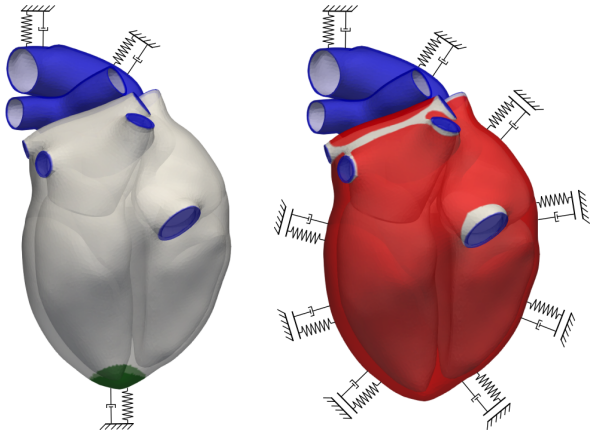

(a) Case *apex* with omni-directional spring-dashpots on Γ^{apex} (green).

(b) Case *pericardium* with normal spring-dashpots on Γ^{epi} (red).

Fig. 8: Surface definitions for boundary conditions with omni-directional spring-dashpots on Γ^{vess} (blue) and homogeneous Neumann boundary conditions (white).

2.6 Solving the 0D-3D coupled problem

We solve the coupled 0D-3D model with the structural and windkessel residuals $\mathbf{R}^{\text{S}}$ and $\mathbf{R}^{\text{0D}}$, respectively, at time step $n+1$ with the Newton-Raphson method

$$\begin{bmatrix} \frac{\partial \mathbf{R}^{\text{S}}}{\partial \mathbf{d}} & \frac{\partial \mathbf{R}^{\text{S}}}{\partial \mathbf{p}} \\ \frac{\partial \mathbf{R}^{\text{0D}}}{\partial \mathbf{d}} & \frac{\partial \mathbf{R}^{\text{0D}}}{\partial \mathbf{p}} \end{bmatrix}_{n+1}^{i} \cdot \begin{bmatrix} \Delta\mathbf{d} \\ \Delta\mathbf{p} \end{bmatrix}_{n+1}^{i+1} = - \begin{bmatrix} \mathbf{R}^{\text{S}} \\ \mathbf{R}^{\text{0D}} \end{bmatrix}_{n+1}^{i}, \tag{25}$$

in a monolithic fashion for increments in displacements and windkessel variables $\Delta\mathbf{d}_{n+1}$ and $\Delta\mathbf{p}_{n+1}$, respectively, at iteration $i+1$ until convergence. We build and solve this coupled system using our in-house code BACI [58]. The numerical parameters for the time integration of our model are listed in table 1d.

3 Results

In order to investigate the influence of pericardial boundary conditions, we compare simulations with and without pericardial boundary condition on the epicardial surface Γ_0^{epi}. The simulations will be denoted by *apex* and *pericardium* in the following. See table 2a for an overview of used parameters.

Case *apex* depicted in figure 8a yields the boundary-vale problem

$$0 = \delta\Pi + \int_{\Gamma^{\text{apex}}} [k_a \boldsymbol{u} + c_a \dot{\boldsymbol{u}}] \cdot \delta\boldsymbol{u} \, \mathrm{d}A \tag{26}$$

adding the energy for omni-directional spring dashpots to the energy (6), where Γ^{apex} is the apical surface. The apical surface is defined as the epicardial surface within 10 mm of the apex, see figure 8. It resembles homogeneous Neumann boundary conditions on $\Gamma_0^{\text{epi}} \setminus \Gamma_0^{\text{apex}}$, i.e. the absence of any pericardial boundary conditions as frequently found in literature [28,25,31].

Case *pericardium* depicted in figure 8b yields the boundary-vale problem

$$0 = \delta\Pi + \int_{\Gamma^{\text{epi}}} \boldsymbol{N} \left[k_p \boldsymbol{u} \cdot \boldsymbol{N} + c_p \dot{\boldsymbol{u}} \cdot \boldsymbol{N}\right] \cdot \delta\boldsymbol{u} \, \mathrm{d}A \tag{27}$$

adding the energy for the pericardial boundary condition to the energy (6), where Γ^{epi} is the pericardial surface. The choice of parameters k_v and c_v is detailed in appendix 3.2.

The remainder of this section is structured as follows. We first give an overview of all methods used in this work to quantify the difference of simulation and MRI in section 3.1. Next, we calibrate model parameters for both cases in section 3.2. In the following sections, we validate various outputs of both simulation cases *apex* and *pericardium* with measurements from cine MRI. We begin with scalar windkessel outputs and compare the simulation volume curves to MRI in section 3.4. A qualitative evaluation of displacement results is given in section 3.5 by comparing end-systolic simulation results to cine MRI frames at multiple views. We quantify the differences in pumping motion for simulation cases *apex* and *pericardium* by comparing the displacements of the left and right atrioventricular plane

to MRI in section 3.6. The interplay between ventricles and atria with and without the presence of pericardial boundary conditions is investigated in section 3.7. In section 3.8 we calculate a spatial error for the left and right endocardium to quantify the overall approximation quality. Finally, we evaluate the contact stress of our pericardial boundary condition of case *pericardium* in section 3.9.

3.1 Assessment of cardiac function

In this section, we briefly describe the various methods we use throughout this work to quantify cardiac function of different simulations.

Cine MRI We use cine MRI with a temporal resolution of ∼30 ms in four- (figure 9a), three-, and two-chamber views and short axis planes with a slice distance of 8 mm (figures 9c, 9d, 9b). All cine MRI data used in this work is rigidly registered to the static 3D image taken during diastasis and used for geometry creation to account for any movement of the subject during image acquisition.

It is important to note that the reference configuration of our simulation is obtained from static 3D imaging with a fine isotropic resolution and acquired in free-breathing, as explained in section 2.2. For the comparison of simulation results to cine MRI however, we have to rely on sparsely distributed images acquired in expiration breath-hold. The used image types rely on different MRI acquisition parameters and pulse sequences. Therefore, it is impossible for our simulation to match the cine MRI data perfectly, even in reference configuration. This error however is usually smaller than the approximation error of the cardiac model.

Left ventricular volume We obtain a reference for left ventricular volume by manually segmenting the left endocardial surface obtained from the short axis cine MRI stack at all time steps. We add the sum of areas in each short axis slice multiplied by the slice thickness. We cut the volume at the top and bottom according to the limits of the left ventricle at each time step, as observed in two chamber and four chamber views.

In order to be fair and not introduce a bias towards our more realistic model, for each simulation, we calibrate the contractility σ_0. It is a key parameter describing cardiac elastodynamics, resembling the asymptotical active fiber stress in (13). It controls maximum deformation during systole. In order to make simulations comparable, we adapt σ_0 for each combination of boundary condition and fiber orientation to match the left ventricular volume at end-systole as segmented from cine MRI of $V_{\text{min}} = 57$ ml. The heart thus yields a stroke volume of 75 ml and an ejection fraction (EF) of 57%.

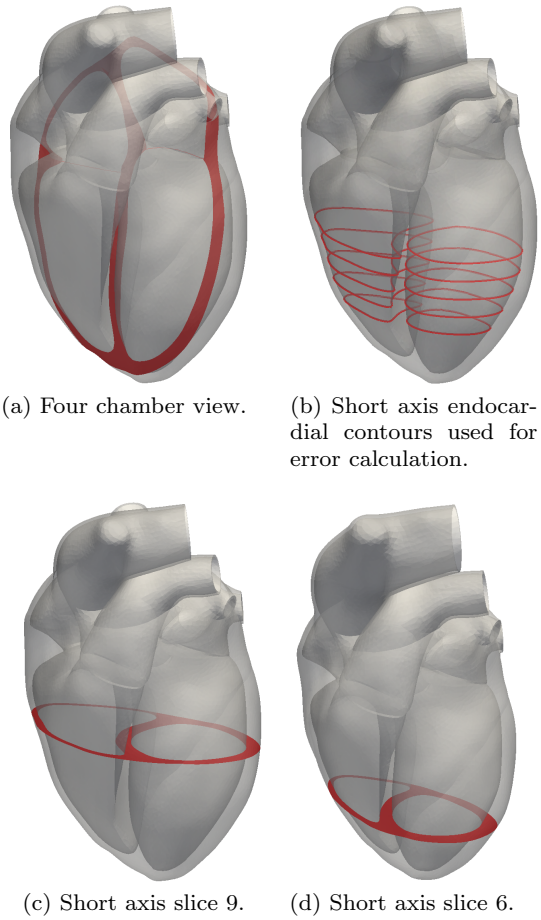

(a) Four chamber view. (b) Short axis endocardial contours used for error calculation.

(c) Short axis slice 9. (d) Short axis slice 6.

Fig. 9: Post processing planes for simulations and cine MRI.

Atrioventricular plane displacement (AVPD) The movement of the left or right plane of the valve separating atrium and ventricle in long axis direction during the cardiac cycle is described by AVPD. For left and right ventricle those valves are termed mitral and tricuspital valve, respectively. As a scalar parameter, AVPD at end-systole is an important clinical parameter to describe and predict cardiac vitality [59,60].

We evaluate AVPD in this work as it gives us a quantitative measurement of the displacements in long axis direction. We semi-automatically extract the displacement of the left and right atrioventricular plane from two, three, and four chamber cine MRI using the freely available software Segment version 2.0 R5585 [61].

In our simulations, we average the displacements on all nodes on the valve plane (see the red planes in figure 5c) and project them onto the long axis direction. A positive sign indicates a movement of the base towards the apex.

Spatial error We validate displacement in long axis direction using AVPD as measurement. To validate radial displacement we compare the movements of cardiac surfaces in simulations to the ones from short axis cine MRI. For comparison, we select the left and right endocardium, as it shows how pericardial boundary conditions prescribed on the epicardium act on the interior of the domain.

For each MRI time step (temporal resolution ∼30 ms) we select the closest simulation time step (temporal resolution 1 ms). Spatially, we extract the simulations' displacement results at the same positions where the cine MRI slices were acquired. This is possible since we use the MRI scanner's global coordinate system for all images and the simulation. This method can be thought of as taking a virtual cine MRI of the simulation. This yields an Eulerian description of motion, as the observer is fixed in space. The difference of simulated displacements to cine MRI data was used previously, e.g. in [25] to estimate local tissue contractility. Note that this technique does not allow us to track rotations of the left ventricle due to its rotational symmetry.

We manually segment the contours of left and right endocardium from short axis cine MRI for slices 5 to 9 at all MRI time steps, see figure 9b. These slices are selected because the myocardium is recognizable for all MRI time steps and not disturbed by either apex or AVP. The function A converts both MRI and simulated endocardial contours $\boldsymbol{d}^s_{\mathrm{MRI}}$ and $\boldsymbol{d}^s$, respectively, to binary images with a resolution of 1×1 mm^2 for every slice s. We use the Dice metric to compare both binary images

$$\epsilon = 1 - \frac{1}{5}\sum_{s=5}^{9} \frac{2\,|A(\boldsymbol{d}^s_{\mathrm{MRI}}) \cap A(\boldsymbol{d}^s)|}{|A(\boldsymbol{d}^s_{\mathrm{MRI}})| + |A(\boldsymbol{d}^s)|} \in [0,1] \tag{28}$$

where $|\bullet|$ denotes the area of the binary image.

Ventricular-atrial interaction Utilizing a four chamber geometry allows us to investigate the interaction between ventricles and atria. Specifically, we want to study the influence of ventricular contraction on atrial filling. We therefore analyze atrial volumes over time. Furthermore, we segmented left and right atrial volumes at ventricular diastasis and end-systole from isotropic 3D MRI.

Pericardial contact stress We evaluate the stresses transmitted between the epicardial boundary conditions and the myocardium for both cases *apex* and *pericardium*. We use different averaged stresses for both cases to quantify the constraining effect of each boundary condition. In case *apex* the stresses are concentrated on the small apical area and acting in any direction. We thus integrate the stress vectors of the apical boundary condition over the apical surface and normalize by the apical area to obtain the mean apical stress

$$\bar{\boldsymbol{t}}_{\mathrm{apex}}(t) = \frac{\int_{\Gamma^{\mathrm{apex}}} \boldsymbol{t}_{\mathrm{apex}}\,\mathrm{d}a}{\int_{\Gamma^{\mathrm{apex}}} 1\,\mathrm{d}a}, \quad \boldsymbol{t}_{\mathrm{apex}} = k_a\boldsymbol{u} + c_a\dot{\boldsymbol{u}}. \tag{29}$$

In case *pericardium* the boundary stresses are distributed over the whole epicardial surface and acting only in normal direction. Therefore, we extract the (signed) normal component t_{epi} and integrate it over the epicardial surface to obtain the mean pericardial stress

$$\bar{t}_{\mathrm{epi}}(t) = \frac{\int_{\Gamma^{\mathrm{epi}}} t_{\mathrm{epi}}\,\mathrm{d}a}{\int_{\Gamma^{\mathrm{epi}}} 1\,\mathrm{d}a}, \quad t_{\mathrm{epi}} = k_p\boldsymbol{u}\cdot\boldsymbol{N} + c_p\dot{\boldsymbol{u}}\cdot\boldsymbol{N}, \tag{30}$$

normalized by the epicardial area.

3.2 Selection of pericardial paramaters

Since in case *apex* the purpose of the apical boundary condition is fixing the apex throughout cardiac contraction, we chose a high spring stiffness permitting only little motion. For case *pericardium*, the parameters k_p and c_v describing pericardial stiffness and viscosity, respectively, need to be calibrated. The chosen value for pericardial viscosity has on its own, i.e. without parallel spring, only little influence on cardiac dynamics. However, in combination with the spring, it prevents unphysiological oscillations of the heart. Pericardial stiffness controls the amount of displacement perpendicular to the epicardial surface and thus the radial motion of the myocardium.

We investigate in the following the influence of the parameter k_p on the contraction of the heart. For this study, we limit ourselves to the $\pm 60°$ fiber distribution, as it is commonly used in cardiac simulations, see e.g. [25,62,37]. We tested the following parameter values:

$$k_p \in \{0.1, 0.2, \ldots, 1.0, 1.5, \ldots, 5.0\} \left[\frac{\mathrm{kPa}}{\mathrm{mm}}\right] \tag{31}$$

For each choice of k_p, we calibrated active stress to yield the same end-systolic volume as measured from MRI.

All parameters except k_p are kept constant throughout this study. Specifically, we did not adjust the timing of ventricular systole to match the volume curve from MRI. However, since all simulations reach the end-systolic state it will be used in this section for quantitative comparisons.

The results of the calibration are shown in figure 10, where maximum active stress is plotted against pericardial stiffness. For comparison, the result for case *apex* with ±60° fibers is included. Active stress required to yield identical end-systolic volume rises strongly with increasing pericardial stiffness. The temporal maximum of pericardial contact stress averaged over the epicardium also increases strongly with k_p, as shown in figure 11. For high k_p, contact stress has the same order of magnitude as active stress and exceeds maximum left ventricular pressure. For small k_p, it has the same order of magnitude as atrial pressure, which experimentally shown to be a good predictor for pericardial contact stress [20].

Figure 12 shows the volume within the pericardial cavity, calculated as the combined volume of all tissue inside the pericardium and the volume within the four cardiac cavities. Case *pericardium* yields a lower volume change than case *apex* and decreases further with increasing k_p.

The end-systolic state of the simulations is shown in figure 13 compared to MRI. The images contain all simulated variants for k_p, where the color changes continuously from $k = 0.1\,\mathrm{kPa/mm}$ (blue) to $k = 5.0\,\mathrm{kPa/mm}$ (red). All MRI views in figure 13 show clearly that pericardial stiffness controls radial displacement of the epicardium. High stiffness values result in less radial inward motion during ventricular systole than visible in cine MRI and vice versa. This is also well observable in figure 13a for the atria in four-chamber view. The short axis views in figures 13b and 13c additionally show that the interventricular septum is stretched and rotated as compared to MRI for high k_p.

The spatial error at left and right ventricular endocardium is shown in figures 14a and 14b, respectively. The increasing mismatch between simulations and MRI for increasing k_p as visible in figures 13b and 13c is quantified as increasing spatial error.

Left and right AVPD is displayed in figures 14c and 14d, respectively. In the left ventricle, i.e. at the mitral valve, AVPD is not very sensitive to the choice of k_p. However, it is higher than in case *apex* but much lower than in MRI. For the right ventricle, i.e. at the tricuspid valve, AVPD is greatly enhanced by increasing k_p towards the value measured in MRI. An identical trend is

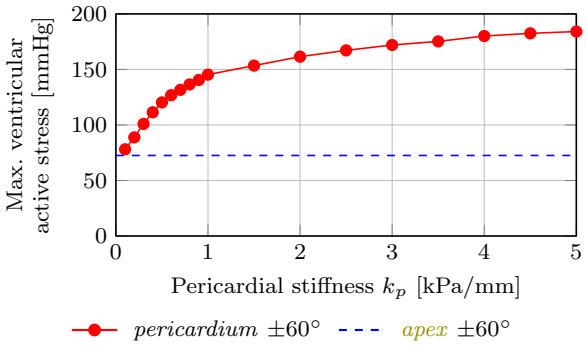

Fig. 10: Maximum ventricular active stress σ_v calibrated to yield identical end-systolic volume. Shown for case *pericardium* with varying pericardial stiffness compared to case *apex*, both with ±60° fiber distributions.

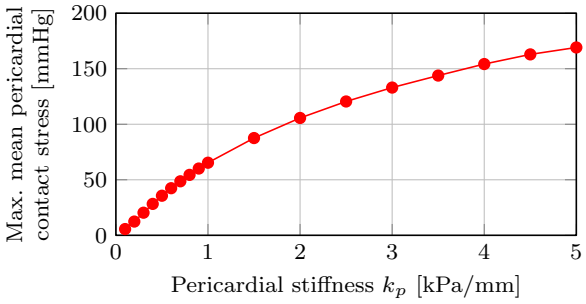

Fig. 11: Maximum of mean pericardial contact stress $\bar{t}_{\mathrm{epi}}$ for case *pericardium* with varying pericardial stiffness and ±60° fiber distributions.

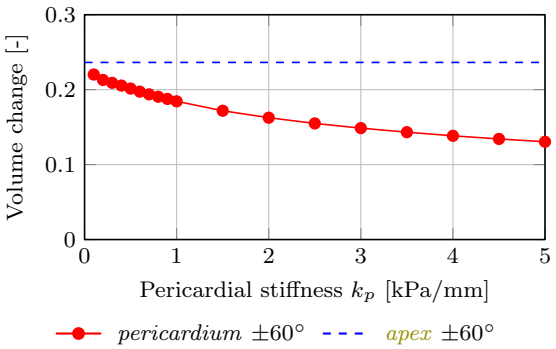

Fig. 12: Volume change for case *pericardium* with varying pericardial stiffness compared to case *apex*, both with ±60° fiber distributions.

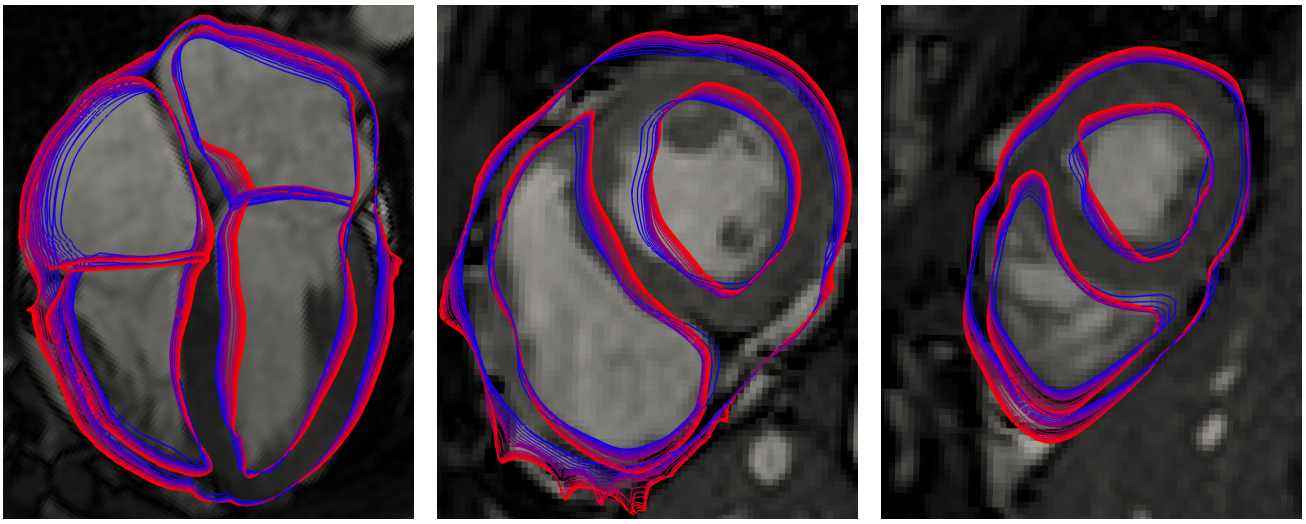

(a) Four chamber view (b) Short axis view slice 9 (c) Short axis view slice 6

Fig. 13: Cine MRI at end-systole for case *pericardium* with ±60° fiber distribution from $k_p = 0.1$ (blue) to $k_p = 5.0$ (red). Views as defined in figure 9. MRI courtesy of R. Chabiniok, J. Harmer, E. Sammut, King's College London, UK.

observable for left and right atrial volume in figures 14e and 14f, respectively.

To conclude the parametric study for pericardial stiffness, we choose for all following simulations the value $k_p = 0.2\,\text{kPa/mm}$. It offers a low spatial error at the ventricles but has higher atrial volume and AVPD than the simulation with $k = 0.1\,\text{kPa/mm}$.

3.3 Model personalization

All simulations are carried out in the following using three different fiber distributions, i.e. ±50°, ±60°, and ±70°. The results for the calibration of σ_0 are shown in table 2b. Note that we show here the maximum value σ_v of active stress instead of σ_0. It can be observed that σ_v is larger in case *pericardium* than in case *apex*. Furthermore, σ_v increases from ±50° to ±70° fibers for more vertical fiber distributions.

The onset of systole and diastole, t_sys and t_dias, as well as the myofiber activation and deactivation rates, α_max and α_max, are adapted to the left ventricular volume curve for ventricles and atria. Here, parameters for the atria are fitted from the interval $t \in [0, 0.2\,\text{s}]$ and $t \in [0.2\,\text{s}, 0.9\,\text{s}]$ for the ventricles. The material parameter η controlling the viscosity of the tissue is fitted during ventricular diastole, i.e. $t \in [0.5\,\text{s}, 0.9\,\text{s}]$. Since active stress is zero during this interval, viscosity controls the relaxation speed of the model. A summary of all calibrated model-specific material parameters is given in table 2. For parameters identical in all models see table 1.

	Γ_0^apex		Γ_0^epi	
	k_a $\left[\frac{\text{kPa}}{\text{mm}}\right]$	c_a $\left[\frac{\text{kPa·s}}{\text{mm}}\right]$	k_p $\left[\frac{\text{kPa}}{\text{mm}}\right]$	c_p $\left[\frac{\text{kPa·s}}{\text{mm}}\right]$
apex	$1.0 \cdot 10^3$	$1.0 \cdot 10^{-2}$	0	0
pericardium	0	0	0.2	$5.0 \cdot 10^{-3}$

(a) Spring stiffness and dashpot viscosity on apical and epicardial surface.

	σ_v [kPa]			t_sys [ms]		
	±50°	±60°	±70°	±50°	±60°	±70°
apex	63.5	72.4	91.0	143	155	172
pericardium	79.4	90.7	129	161	170	193

(b) Maximal myocardial active stress σ_v and ventricular activation time t_sys.

Table 2: Calibrated parameters for simulation cases *apex* and *pericardium* and different fiber orientations.

3.4 Scalar windkessel results

Firstly, in figure 15 we compare the scalar outputs volume (left) and pressure (right) of the left ventricle of our windkessel model. As explained in section 3.2, the contractility σ_0 was calibrated in all simulations to match end-systolic volume as segmented from cine MRI. Therefore, in figures 15a and 15c the volumes of MRI and all simulations match at $t = 0.51$ s. Furthermore, although

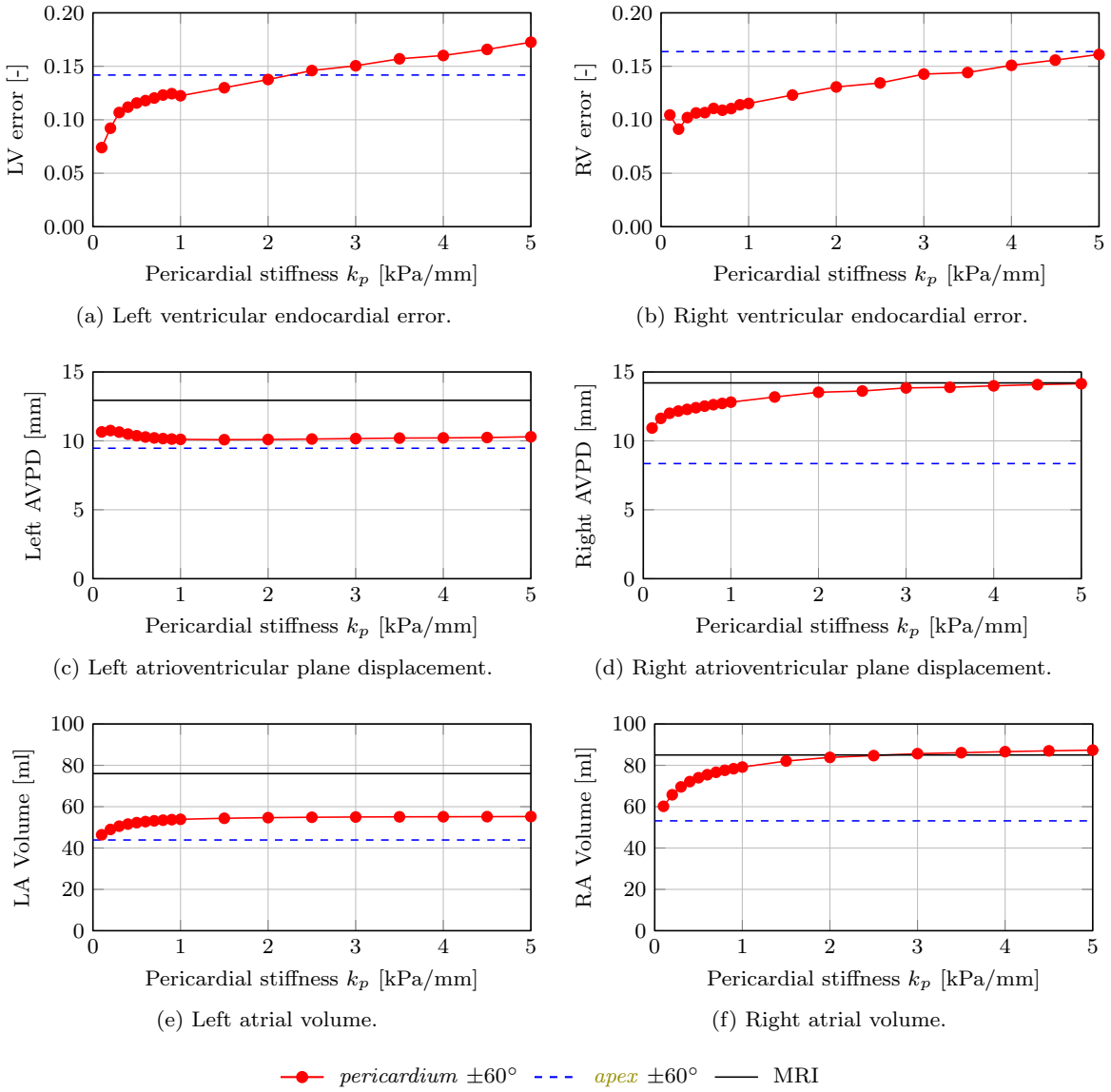

(a) Left ventricular endocardial error.

(b) Right ventricular endocardial error.

(c) Left atrioventricular plane displacement.

(d) Right atrioventricular plane displacement.

(e) Left atrial volume.

(f) Right atrial volume.

Fig. 14: Kinematic scalar cardiac quantities at end-systole for case *pericardium* with varying pericardial stiffness $k_p \in [0.1, 5.0]$ compared to case *apex* both with ±60° fiber distributions and MRI.

they result from simulations with very different boundary conditions and fiber orientations the volume curves are very similar. The maximum volume due to atrial contraction and the prescribed atrial pressure in figure 7b is similar in both cases but lower than in MRI. As for the volume curves, the pressure curves in figures 15b and 15d are remarkably similar despite the different simulation settings. Because case *pericardium* exhibits a faster decay in volume during systole than in case *apex*, the pressure peak during systole is more pronounced.

3.5 Displacements at end-systole

As demonstrated in section 3.4, the results of the scalar output parameters left ventricular volume and pressure are mostly invariant to changes in boundary conditions or fiber orientation. Validating the elastodynamical model of cardiac contraction thus requires a comparison of displacement results to spatially distributed MRI observations, see figure 16. The reference configuration (diastasis) of the simulation is shown in figures 16a, 16b, 16c. We compare the MRI frames at end-systole to our simulation results using the four chamber view, see figures 16d and 16g, and two different short

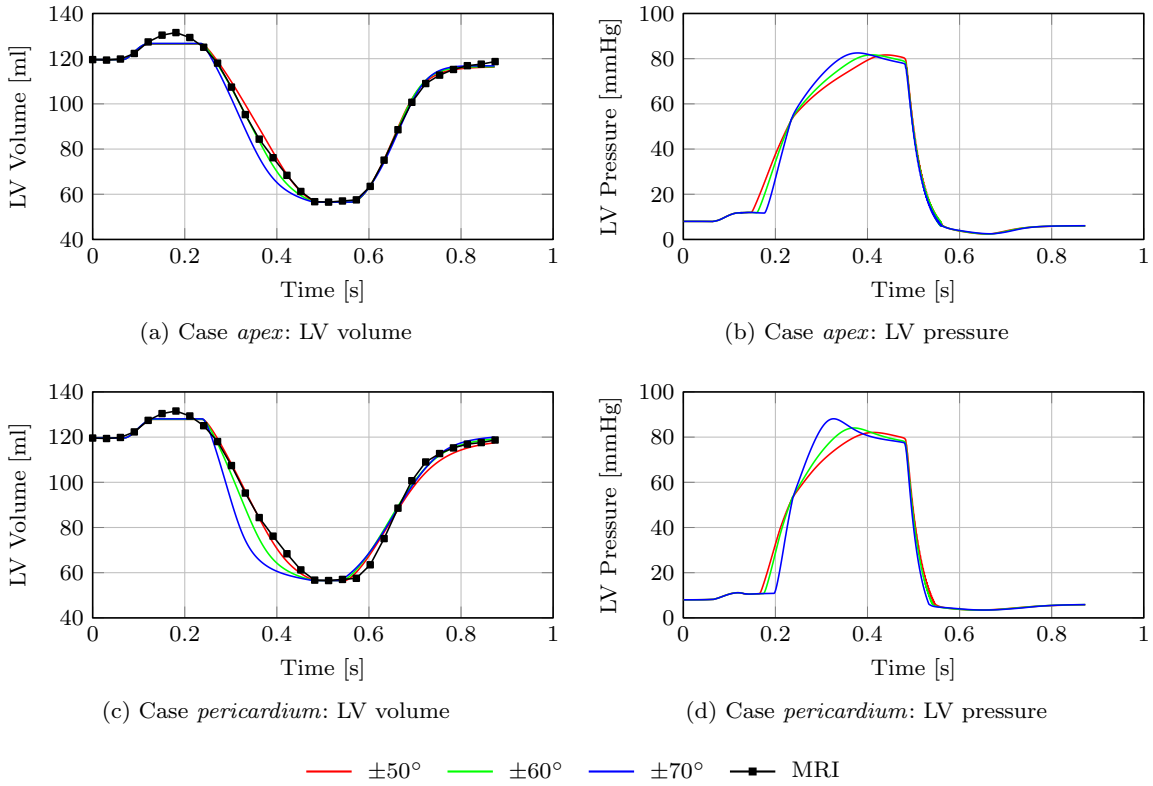

(a) Case *apex*: LV volume

(b) Case *apex*: LV pressure

(c) Case *pericardium*: LV volume

(d) Case *pericardium*: LV pressure

Fig. 15: Simulation results for volume (left) and pressure (right) of the left ventricle (LV) for boundary condition cases *apex* (top) and *pericardium* (bottom). Volume results are compared to cine MRI.

axis views, see figures 16e, 16h, 16f, 16i. The location of the view planes is visualized in figures 9a, 9c, 9d.

For case *apex*, there is a radial inward movement of the myocardial wall. In figure 16d, this is especially visible at right atrial free wall and at the left and right epicardial free wall. There is a large mismatch between simulation and MRI at the interatrial septum. Due to the radial contraction motion, atrioventricular plane displacement (AVPD) is lower than in MRI. The fixation of the apex in case *apex* causes a mismatch between simulations and MRI at the apex, as the apex slightly moves during cardiac contraction. The interventricular septum's matches well with MRI in figures 16e and 16f. However, the mismatch of epicardial contours is clearly visible and sensitive to fiber orientation.

Comparing figures 16d and 16g, the influence of the pericardial boundary condition becomes clearly visible. It can be observed for case *pericardium* in figure 16g that the epicardial contour matches the MRI much closer than case *apex* in figure 16d for any fiber orientation. The movements of the left and right atrioventricular plane also match well with MRI, for both orientation and displacement in normal direction. The displacements at the apical region are also predicted more accurately than in case *apex*. Comparing the shape of the right ventricle in figures 16d and 16g, one can observe that the pumping motion of the right ventricle in case *apex* is the result of radial movement, whereas in case *pericardium* it is the result of a downward movement of the atrioventricular plane. The same observation holds for a less visible degree for the left ventricle. Through the constraining effect of the pericardium, the atria are visibly more stretched than in case *apex*. There is also an influence of the fiber orientation in case *pericardium*, although it is more bound to the endocardial surfaces. The more vertical the fiber orientation, i.e. from ±50° (red) to ±70° (blue), the larger the displacements of the atrioventricular planes and the smaller the displacement of the apex in anterior direction. There are some mismatches between simulation and MRI at the interatrial and interventricular septum but less pronounced than in case *apex*. The deviation at the interventricular septum can be observed for short axis slice 9 in figure 16h. For short axis slice 6 in figure 16i there is a good agreement with simulation and MRI at all regions of the left and right myocardium.

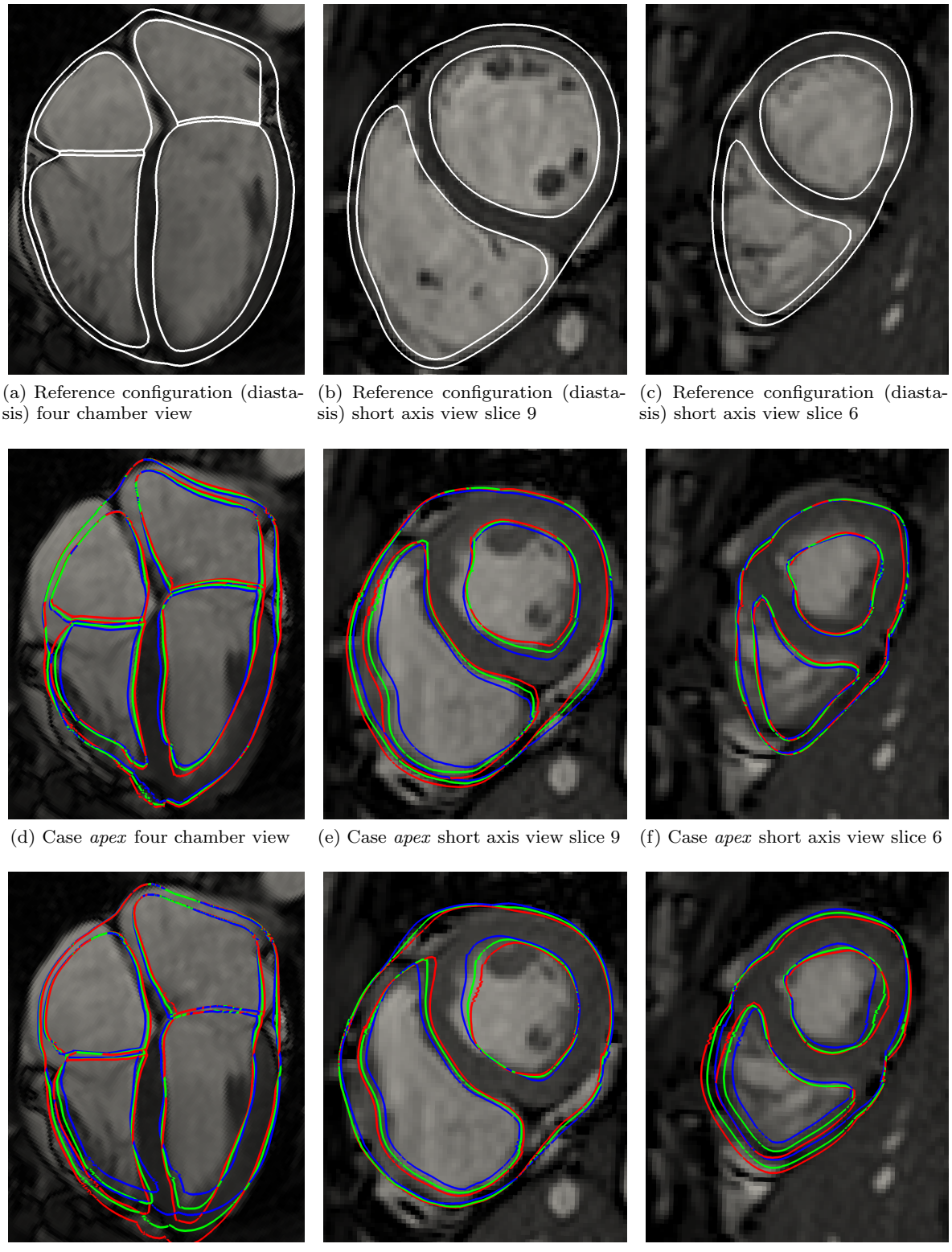

(a) Reference configuration (diastasis) four chamber view

(b) Reference configuration (diastasis) short axis view slice 9

(c) Reference configuration (diastasis) short axis view slice 6

(d) Case *apex* four chamber view

(e) Case *apex* short axis view slice 9

(f) Case *apex* short axis view slice 6

(g) Case *pericardium* four chamber view

(h) Case *pericardium* short axis view slice 9

(i) Case *pericardium* short axis view slice 6

Fig. 16: Reference configuration (diastasis) as well as simulation results and cine MRI at end-systole in four chamber view and short axis views as defined in figure 9. MRI courtesy of R. Chabiniok, J. Harmer, E. Sammut, King's College London, UK

3.6 Atrioventricular plane displacement

The AVPDs of simulations and MRI are compared in figure 17. The left and right AVPD from MRI (black) is zero at the beginning and at the end of the cardiac cycle. During atrial systole, the left and right atriovencular planes (AVP) move away from the apex and reach both their minimal value at atrial end-systole at $t = 0.17s$. Followed by ventricular systole, the AVPs move towards the apex and both reach their maximal value at ventricular end-systole at $t = 0.51s$.

During atrial systole for $t \in [0, 0.25s]$, negative AVPD, i.e. movement of the AVP towards the atria, is less pronounced and delayed in both cases as compared to MRI. However, extremal AVPD at atrial end-systole is slightly higher in case *pericardium* than in case *apex*.

Comparing AVPD cases *apex* and *pericardium* in figures 17a, 17c, 17b, 17d, one can observe that in both cases maximum AVPD depends on fiber orientation: Maximum AVPD increases from horizontal $\pm 50°$ fibers (red) to vertical $\pm 70°$ fibers (blue). The dependence on fiber orientation is more pronounced in case *apex* than in case *pericardium*. In general, AVPD is slightly higher in case *pericardium* than in case *apex* but still underestimates measurements from MRI.

3.7 Ventricular-atrial interaction

Atrial systole is visible by the drop in atrial volume in both cases. Passive atrial filling is non-existent in case *apex*, as the volume in figures 18a and 18b stay constant during ventricular systole. This is also visible at the end-systolic four-chamber view in figure 16d. For $\pm 70°$ fibers, the right atrium is even slightly emptied during ventricular systole, as observed in figure 18b. Atrial filling can be observed for case *pericardium* in figures 18c and 18d. Both atria are visibly filled during ventricular systole, although maximum atrial volume remains smaller than in MRI.

3.8 Spatial error

For case *apex* in figures 19a and 19b the error is lowest in both ventricular endocardia during contraction at end-systole at $t = 0.51$. The error rises during ventricular contraction and relaxation. Errors at the end of the simulation higher than the ones at $t = 0$ suggest that the state at the end of the simulation differs from the reference configuration. The overall error is much lower in case *pericardium* than in case *apex*.

3.9 Boundary stresses

Both scalar boundary stresses $\bar{t}_{\text{apex}} = \|\bar{\boldsymbol{t}}_{\text{apex}}\|_2$ and $\bar{t}_{\text{epi}}$ are visualized in figure 20 over time for all fiber orientations. It can be observed that apical stress in case *apex* is orders of magnitude higher than pericardial stress in case *pericardium* and more dependent on fiber orientation. Positive values of $\bar{t}_{\text{epi}}$ indicate predominant tensile stresses between epicardium and pericardium. It can be seen that mean pericardial stress in figure 20b is a compressive stress for most of the cardiac cycle, except at the end of systole and onset of diastole.

Boundary stresses are visualized in figure 21. For case *apex*, the mean stress vectors $\bar{\boldsymbol{t}}_{\text{apex}}$ for all three fiber distributions are shown in figure 21a at $t = 0.45$ and scaled according to their magnitude. Fiber orientation has not only a strong influence on the magnitude but also the direction of mean apical stress.

The local distribution of pericardial contact stress with $\pm 60°$ fibers at end-systole is shown in figure 21b in reference configuration. At end-systole, compressive as well as tensile stresses occur. Stresses are centered around a tensile stress of 20 mmHg. Areas of high compressive stresses are at the left atrium, the anterior and posterior right ventricle, the posterior left ventricle, and the anterior left ventricular apex. Areas of high tensile stresses are the right ventricle close to the anterior part of the right ventricular outflow tract and the left and right ventricular free wall. Overall, pericardial contact stress is evenly distributed around the epicardial surface.

4 Discussion

Our objective was to analyze the effects of the pericardial boundary condition proposed in section 2.1 based on the physiology of the pericardium, comparing simulation cases *pericardium* and *apex*. We first performed a parametric study to explore the influence of pericardial stiffness. Each simulation case was then personalized and evaluated for the fiber orientations $\pm 50°$, $\pm 60°$, and $\pm 70°$. We then compared scalar left ventricular pressure and volume. The displacements at end-systole were qualitatively compared to multi-view cine MRI. Additionally, we quantified the differences of both simulation cases to MRI by atrioventricular plane displacement (AVPD), passive atrial filling, and spatial approximation error at the left and right ventricular endocardium.

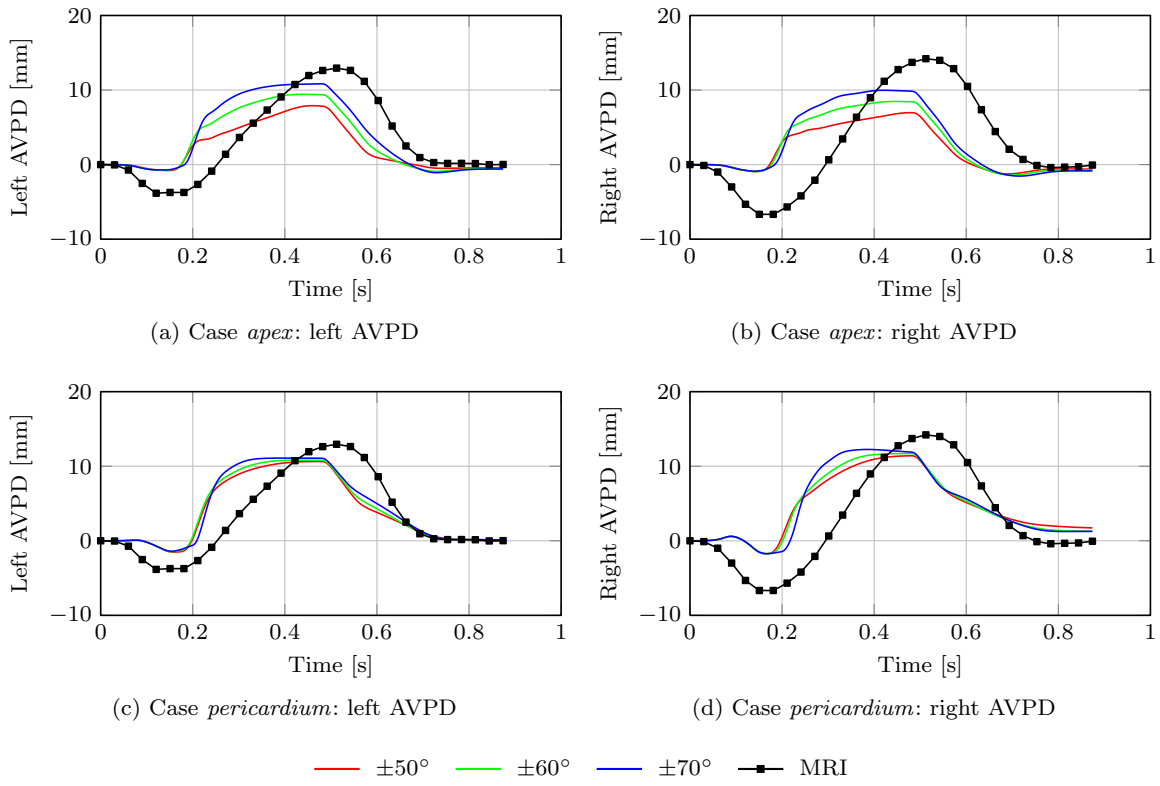

(a) Case *apex*: left AVPD

(b) Case *apex*: right AVPD

(c) Case *pericardium*: left AVPD

(d) Case *pericardium*: right AVPD

Fig. 17: Simulated atrioventricular plane displacement for left and right ventricle compared to cine MRI.

4.1 Pericardial stiffness

The parametric study for pericardial stiffness in case *pericardium* in section 3.2 revealed that the ventricles are well approximated by the lowest tested stiffness values, e.g. $k_p = 0.1\,\text{kPa/mm}$. Here, the error at left and right ventricular endocardium was minimized and much lower than in case *apex*.

In contrast, right AVPD and right atrial passive filling matched well with measurements from MRI for high stiffness values, e.g. $k_p = 3.0\,\text{kPa/mm}$. Choosing this value globally for pericardial stiffness lead however to some undesirable consequences, namely unphysiologically high myocardial contractility and pericardial stress as well as bad approximation of the interventricular septum.

In future studies, it might thus be reasonable to select spatially varying pericardial parameters. This hypothesis is supported by the fact that the pericardial tissue is in contact with various organs of different material properties as outlined in section 1.2.2. A starting point could be the estimation of regional pericardial parameters based on the surface definitions in figure 2 with the objective to match MRI measurements in section 3.2.

In case of a biventricular geometry, no atria are present. Thus AVPD is not controlled by the interaction of atria and pericardium. Furthermore, atrial filling is not taken into account. We thus expect that a global value of $k_p = 0.1\,\text{kPa/mm}$ for pericardial stiffness yields good results for a biventricular geometry with ±60° fibers. This value was also used in [37], although it was not really analyzed there, e.g. with respect to MRI.

4.2 Pumping mechanism

We calibrated cardiac contractility in all simulations in section 3.2 to yield the same end-systolic volume. It was shown that in case *pericardium*, higher contractilities are required than in case *apex*. Therefore, for a given contractility, a heart constrained with the pericardial boundary condition yields less output. This result is in agreement with the experimental observation that cardiac output is greatly increased after the removal of the pericardium [15]. The result further agrees with the numerical experiments performed in [34]. For identical active stress, left ventricular ejection fraction decreased from 71 % to 63 % when including the pericardium.

The main pumping mechanism of the heart is shortening in long axis direction, which is quantified by AVPD

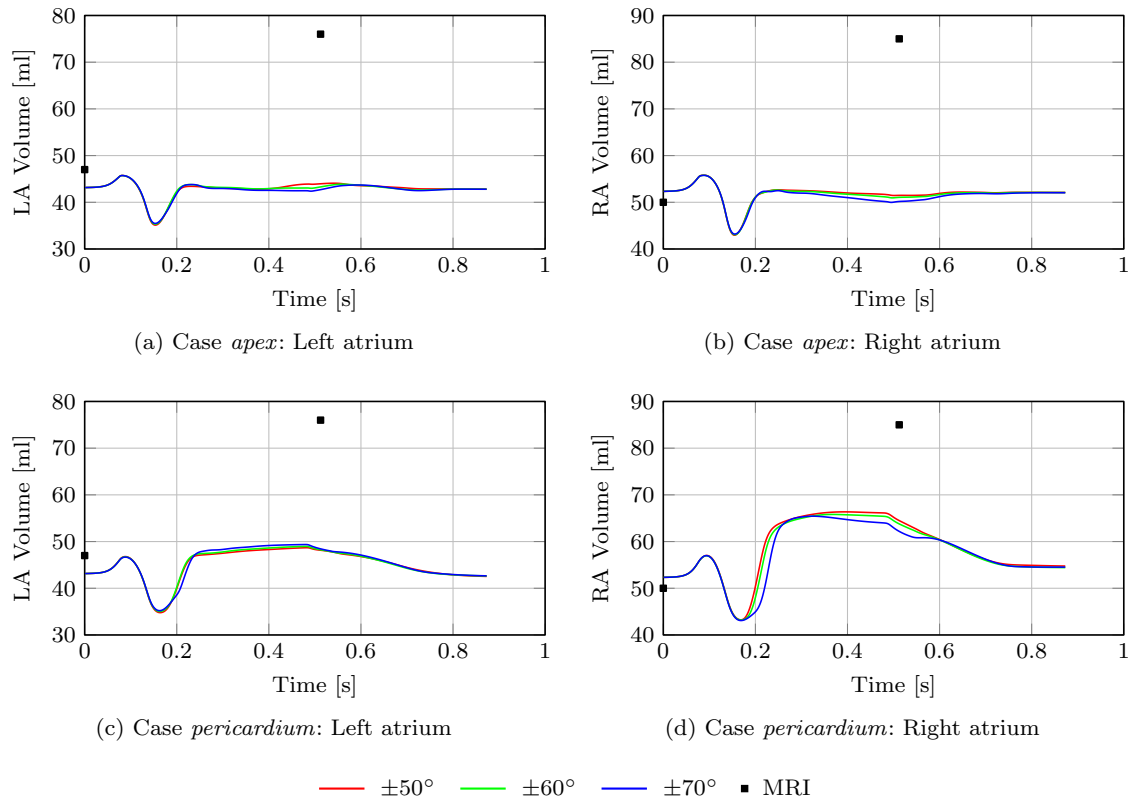

(a) Case *apex*: Left atrium

(b) Case *apex*: Right atrium

(c) Case *pericardium*: Left atrium

(d) Case *pericardium*: Right atrium

Fig. 18: Simulated volume curves for left and right atrium compared to 3D MRI at ventricular diastasis and end-diastole.

[63,64]. In [65], the pumping function of the heart was compared to a piston unit with the AVP as a piston. This mechanism could be observed in section 3.6 for case *pericardium*, where left and right AVPD is higher than in case *apex* but still lower than in MRI.

The upper part of the left atrium is fixated by pulmonary veins. Ventricular contraction forces the mitral ring towards the apex and promotes the filling of the left atrium from the pulmonary veins [66]. In section 3.7 we compared atrial filling during ventricular systole with and without pericardium. It was observed that the simulations of case *pericardium* which promoted higher AVPD in section 3.6 contribute more to atrial filling during ventricular systole. Case *pericardium* predicts maximal atrial volume at ventricular end-systole as segmented from isotropic 3D MRI better than case *apex*. The simulated values are however still lower than in MRI for the chosen pericardial parameters.

Keeping in mind that all simulations yield the same end-systolic volume, it was shown that the pumping mechanism of the heart is very different for cases *apex* and *pericardium* although their pressure and volume curves were similar in section 3.4. Comparison of four-chamber and short axis slices of the left and right ventricle from simulation results to cine MRI in section 3.5 revealed an unphysiological radial pumping motion without pericardial boundary conditions in case *apex*. In [67] it was found that the outer diameter of the left ventricle shortens only about 2 mm during systole. Furthermore, the total volume enclosed by the pericardium changes only by about 5-8 % during the cardiac cycle [68,64]. We found that for the ±60° fiber orientation the total change in pericardial volume is 24 % and 21 % for cases *pericardium* and *apex*, respectively. This mismatch is mainly due to the unphysiological change in atrial volume during ventricular contraction.

As demonstrated in the parametric study in section 3.2, AVPD and atrial filling could be increased to the values measured in MRI by increasing the global pericardial stiffness. However, this was shown to lead to a worse approximation of the interventricular septum. This motivates the use of a regionally distributed pericardial stiffness. Another reason for underestimating AVPD and atrial filling might be an atrial material model, which is in our case identical to the ventricular one, that is too stiff.

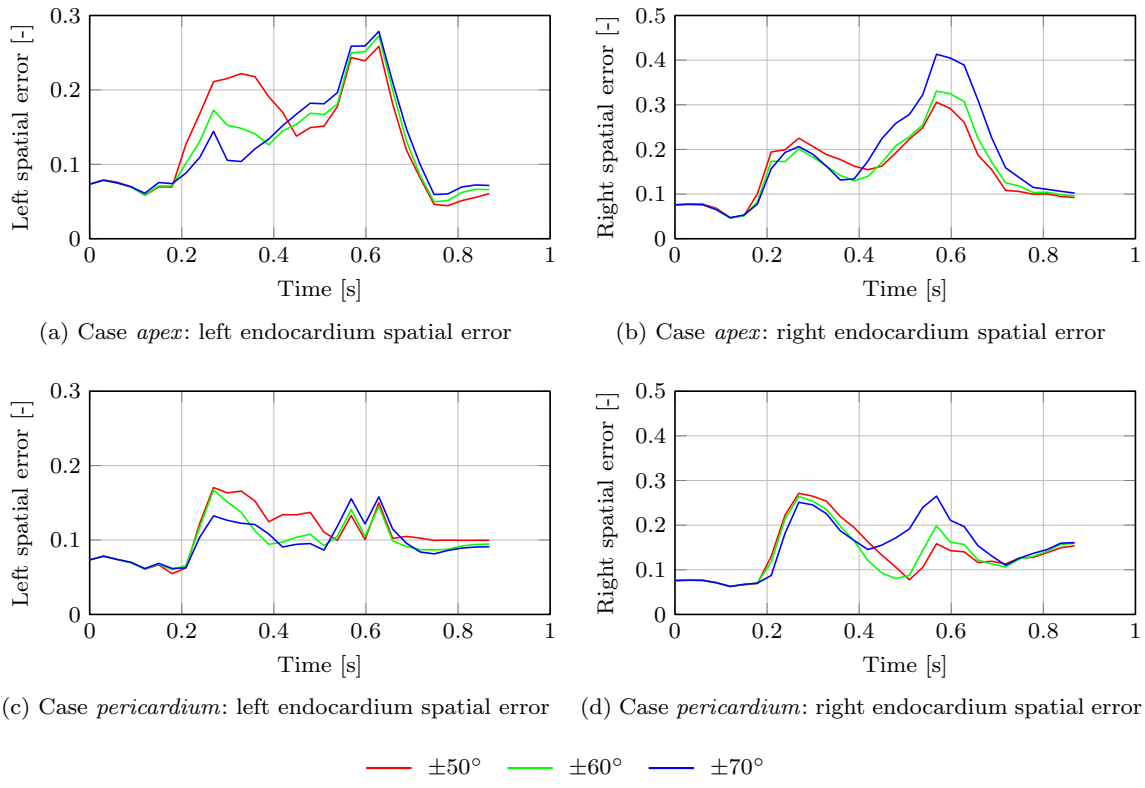

(a) Case *apex*: left endocardium spatial error

(b) Case *apex*: right endocardium spatial error

(c) Case *pericardium*: left endocardium spatial error

(d) Case *pericardium*: right endocardium spatial error

Fig. 19: Relative spatial error of simulation results and cine MRI at left and right endocardium.

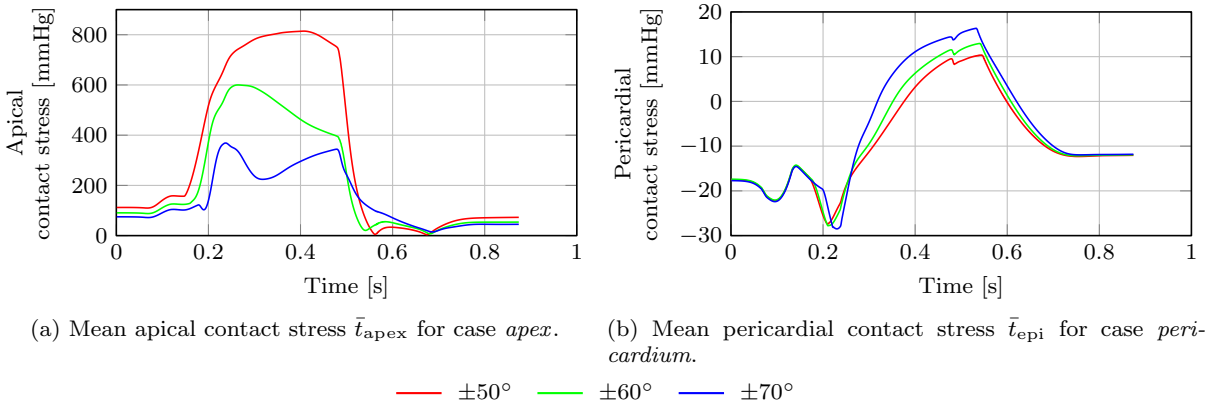

(a) Mean apical contact stress $\bar{t}_{\text{apex}}$ for case *apex*.

(b) Mean pericardial contact stress $\bar{t}_{\text{epi}}$ for case *pericardium*.

Fig. 20: Boundary condition stress.

4.3 Fiber orientation

We compared in this work three fiber orientations within the myocardium, namely ±50°, ±60°, and ±70°. We studied the influence of fiber direction for both boundary conditions cases *apex* and *pericardium*. It was shown that fiber orientation has a strong influence on the displacements. In section 3.6 ±70° fiber orientations exhibited larger AVPD for both boundary condition cases. This can be attributed to the fact that the fiber orientation is more vertical, i.e. more aligned with the long axis, than ±60° and ±50° fiber orientations. Since myofiber contraction is prescribed in fiber direction, more vertical fiber orientations inherently apply a greater force pushing apex and AVP together, thus yielding higher AVPD. Since the AVP is also attached to the atria, AVPD is also linked to atrial filling. In section 3.7 it was shown that the more vertical ±70° fiber orienta-

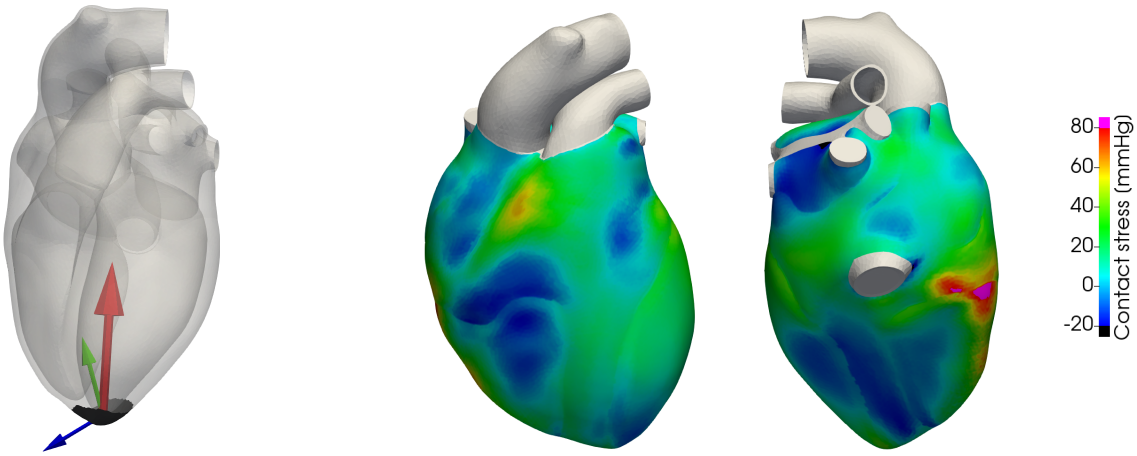

(a) Case *apex* mean apical stress vectors $\bar{\boldsymbol{t}}_{\text{apex}}$ (scaled by magnitude) for ±50° (red), ±60° (green), and ±70° (blue) fiber orientations at $t = 0.45$.

(b) Case *pericardium* pericardial contact stress t_{epi} on epicardial surface with ±60° fibers at end-systole $t = 0.51$.

Fig. 21: Visualization of boundary stresses.

tion also yielded the highest atrial filling during ventricular systole. Comparing results to short axis cine MRI slices, it was shown that a more horizontal ±50° fiber orientation leads to a more radial contraction of the heart. The maximum pericardial stress at end-systole was highest for ±50° fibers. This can be explained by the observation in figure 16h where ±50° fibers (red) exhibited the most radial inward movement during systole. Since the myocardial-pericardial interface can only transmit forces in normal direction, a more radial contraction exerts a higher pericardial tensile stress. The overall spatial approximation error was also shown to be dependent on fiber direction. However, the dependence was more pronounced in case *apex* than in case *pericardium*.

4.4 Pericardial contact stress

In [19] end-diastolic pericardial contact pressure was measured with a flat balloon catheter at the left ventricular anterolateral epicardial surface with around 15 mmHg. In vivo experiments on humans in [20] showed pericardial pressures on the left lateral surface of the heart between 0 and 15 mmHg. The prestressing procedure in our model not only includes the myocardium but also the pericardial boundary condition in case *pericardium*. Here, we measure a contact pressure of 20 mmHg at diastasis on the left ventricular epicardial surface, agreeing well with experimental observations.

The stresses exerted by the boundary conditions on the epicardial surface of the heart were found to be over one order of magnitude higher in case *apex* than in case *pericardium*. The exact stress values in case *apex* depend on the choice of apical spring stiffness, which was not calibrated in this study. It is nevertheless evident, that unphysiologically high stresses are concentrated in a very small area of the heart. In case *pericardium*, all boundary stresses are evenly distributed on the epicardial surface.

The similar maximum values of mean pericardial contact stress for all fiber directions in case *pericardium* suggest that pericardial constraint is displacement-controlled. Pericardial constraint is determined by the deviation of the heart throughout the cardiac cycle from its end-diastolic state. However, as outlined in section 1.2.2, to the best of the authors' knowledge there are no measurements of pericadial contact pressure during the cardiac cycle to validate the stresses experienced in our computational study. Pericardial contact stress is thus an output of our computational model which is not yet available in clinical practice. Given that our model was solely calibrated to kinematic data, the pericardial contact stresses predicted by our model should be considered as qualitative results.

4.5 Numerical performance

We ran all simulations on two nodes of our Linux cluster. One node features 64 GB of RAM and two Intel Xeon E5-2680 "Haswell" processors, each equipped with 12 cores operating at a frequency of 2.5 GHz. The

computation time of cases *apex* and *pericardium* was almost identical, which was about 18 hours for each of the simulations performed in this work, including prestressing. The pericardial boundary condition requires little effort to evaluate, since the pericardial boundary condition only requires the displacement field, which is computed anyway, and reference surface normals, which are computed once at the initialization of the simulation. Some differences in numerical performance arise since the calculated displacement fields of both cases are different. Taking the $\pm 60°$ fiber distribution, case *apex* had an average of 7.8 Newton iterations per time step and 28 linear solver iterations per Newton iteration. For case *pericardium*, these values were 8.3 and 25, respectively.

4.6 Limitations and future perspectives

As mentioned earlier, in this work, we did not account for the propagation of the electrical signal sent from the sinus node. Rather, all myocardial tissue in our simulations was activated simultaneously. We recently demonstrated the ability to couple our mechanical model to an electrophysiological model [51], which we can include in further studies. However, since the data came from a healthy volunteer, we do no expect relevant variations.

Ex-vivo experiments on myocardial tissue in [69, 70, 71] showed anisotropic tissue characteristics, depending on myocardial fiber and sheet orientation. In our model, we used the anisotropic material model proposed in [35] for myocardial tissue. Due to the lack of sufficient experimental data, we used identical material properties for left and right myocardium, as well as the atria. However, no studies have been carried out how material parameters obtained from experiments on ex vivo tissue correlate to in vivo material behavior. Furthermore, it should be noted that vastly different material parameters have been estimated in [35] and [72] when being fitted to measurements from either biaxial extension tests or shear tests.

Our structural model was coupled to a lumped-parameter windkessel model of hemodynamics of the systemic and pulmonary circulation with prescribed atrial pressures. The interaction between atria and ventricles should be investigated in further studies using a volume-preserving closed-loop model, including both pulmonary and systemic circulation. Furthermore, none of our cardiac simulations are perfectly periodic, i.e. the values at the end of the cardiac cycle are not equal to the initial conditions. In future studies, achieving a periodic state should be incorporated into parameter estimation.

In this work we interpolated the local helix fiber directions at the integration points from three different prescribed constant-per-surface fiber orientations. Results showed that fiber orientation has a large influence on AVPD. However, we have no knowledge of patient-specific fiber orientation and assumed equal distributions in left and right ventricle. Patient-specific cardiac fiber orientations can be estimated from diffusion tensor MRI [73] (DTMRI). However, while applicable to in vivo DTMRI (as shown in [73]), to the best of our knowledge, fiber estimation has not been tested and validated with in vivo DTMRI yet. Further quantitative studies of cardiac dynamics require a fine resolution of patient-specific fibers.

We further assumed constant stiffness and viscosity parameters of our pericardial boundary condition over the epicardial surface. Given reliable material parameters for the myocardium, constant pericardial stiffness and viscosity could be estimated from measured AVPD. The choice of constant parameters might however be oversimplified, as the pericardium is in contact with various tissues of different mechanical behaviors, as illustrated in figure 2. For example, the movement of the apex in anterior direction in case *pericardium* as observed in figure 16g suggests a higher pericardial stiffness to model the influence of the sternum and the diaphragm. This will however introduce more parameters to the model, which will need to be calibrated to measurements from e.g. cine or 3D tagged MRI. For this study we kept the number of parameters small in order to make evident the general effect of the pericardial boundary condition even by using a simplified modeling approach.

From a machine learning perspective, we split our limited available data from cine MRI into a training set and a test set. The training set data is used during model personalization. The rest of the data can then be used in the test set to check how well the model actually predicts data that was not used during personalization. In our case, we used as training set left ventricular volume and ventricular epicardial contours to tune timing, (de-) activation rates, and contractility for atria and ventricles and global material viscosity and pericardial stiffness. We then used as test set AVPD, atrial volume, and ventricular endocardial contours, each left and right, to quantify the simulations' approximation error. Many more parameters of our cardiac model could be personalized for this patient-specific study. However, using the metrics in our test set for model calibration would disqualify using them to test model accuracy and limit our abilities to test the model.

We validated our simulation results solely with cine MRI data. Cine MRI can be interpreted as an Eule-

rian description of cardiac movement, as the imaging planes stay fixed in space throughout the cardiac cycle. This observation however cannot detect any rotational movement with respect to the long axis, as the left ventricle is almost rotationally symmetric. To properly validate any rotational movement of the myocardium, a comparison to data from 3D tagged MRI is necessary, which can be interpreted as a Lagrangian observation of cardiac motion. Furthermore, pressure measurements from within ventricles and atria are required. Pressure values at end-diastole yield initial values for the stress state of the myocardium, which cannot be assessed from imaging alone. Pressure curves over the cardiac cycle would yield a ground truth to validate the outputs of our windkessel model. Figure 18 demonstrates that the model, while using the pericardial constraint, does predict accurately the atrial volume at ventricular end-systole. However, we have no data available at atrial end-systole. In future studies, if detailed cine data of atria are available (e.g. cine stack in trasverse orientation with respect to the body, and using thin slices of 5mm), we will consider a more detailed analysis of atrial contraction.

4.7 Concluding remarks

In this work we gave an overview of the anatomy and mechanical function of the pericardium and motivated to model its influence on the myocardium as a parallel spring and dashpot acting on the epicardial surface. Following a review of pericardial boundary conditions currently used in mechanical simulations of the heart, we proposed to compare two simulation cases, one with and one without pericardial boundary conditions. Following calibration to stroke volume as measured from short axis cine MRI, we compared several physiological key outputs of our model and validated them using multi-view cine MRI. Although exhibiting similar volume and pressure curves, the displacement results of both simulation cases were radically different. The simulations with pericardial boundary conditions matched MRI measurements much closer than without, especially with respect to atrioventricular plane displacement and atrial filling during ventricular systole, quantities which were not included in the calibration of the model. By establishing an overall spatial approximation error at the left and right endocardium, we showed that the introduction of only two global parameters for the pericardial boundary condition already yields a big gain in model accuracy. Our ultimate goal is to obtain more comprehensive data sets, adding 3D tagged MRI and pressure measurements, to further validate our model of pericardial-myocardial interaction. Measurements of pericardial contact stress at different locations on the epicardium throughout the cardiac cycle would help to test the qualitative predictions of pericardial contact stresses by our model and will probably lead to further model improvements.

Compliance with ethical standards

Conflict of interest The authors declare that they have no conflict of interest.

A Comparison of spring formulations

We show in section 2.1 how the pericardial boundary condition in case *pericardium* can be derived from adhesive sliding contact by introducing several simplifications. To justify the simplifications made by our pericardial boundary condition, we use a very simple geometry of a hollow half-ellipsoid with $\pm 60°$ fibers, which roughly represents the shape of the left ventricle, see figure 22a. It is able to show the consequences of each approach while being simple enough to isolate the effects of the boundary condition. The parameters of the ellipsoid model are given in table 3. We use the same active stress model introduced in (8) to mimic cardiac contraction. All three simulations use the same contractility parameter.

As in section 3, case *pericardium* utilizes the pericardial boundary condition proposed in (5) using the gap (4). Additionally, we introduce case *pseudo-contact*, which uses the definition of the gap in (3) based on projection and the current normal vector to the epicardium. Case *free* has homogeneous zero-Neumann boundary conditions on the whole epicardial surface.

The results of the contraction simulation are shown in figures 22b and 22c at end-systole. Displayed is the reference configuration and all three boundary condition cases for a cross-section of the ellipsoid. Figure 22b shows in a frontal view the shortening of the ellipsoid with visible epi- and endocardial contours. While cases *pericardium* and *pseudo-contact* are very similar with little differences only in radial direction, case *free* exhibits much less longitudinal shortening. There is almost no longitudinal shortening but a translational movement of the whole geometry instead.

Figure 22b shows the epicardial contour of the ellipsoid in a top-down view to observe the twisting motion of the ellipsoid. All three boundary condition cases are very similar. This confirms that the normal springs in cases *pericardium* and *pseudo-contact* in fact allow tangential sliding and do not prohibit any rotational movement, as they are very similar to case *free*. Furthermore, the similarity of cases *pericardium* and *pseudo-contact* shows that the simplified spring formulation (4) in case *pericardium* is sufficient to represent the effects of the pericardium compared to the more detailed formulation (3) in case *pseudo-contact*.

References

1. Iaizzo P. A. *Handbook of cardiac anatomy, physiology, and devices*. Springer Science & Business Media; 2015.

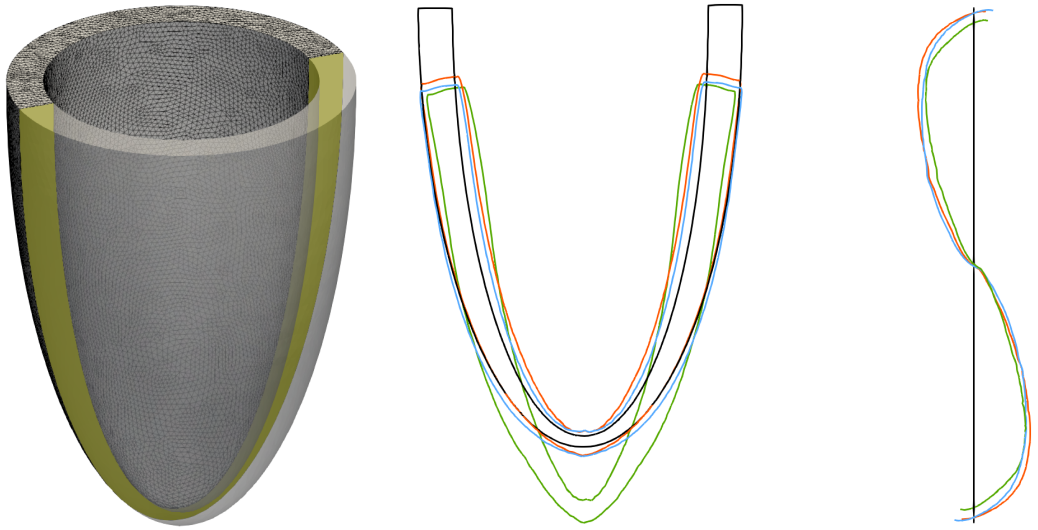

(a) Ellipsoid model in reference configuration with cross-section (yellow).

(b) Frontal view of epi- and endocardial cross-section at end-systole.

(c) Top-down view of epicardial cross-section at end-systole.

Fig. 22: Ellipsoid model in reference configuration (black) with cases *free* (green), *pericardium* (blue), and *pseudo-contact* (orange).

Name	**Par.**	**Value**	**Unit**
Tissue density	ρ_0	10^3	$\left[\frac{\text{kg}}{\text{m}^3}\right]$
Viscosity	η	10	[Pa · s]
Volumetric penalty	κ	10^4	[kPa]
Ventricular contractility	σ_v	185	[kPa]
Mooney-Rivlin	C_1	10	[kPa]
Mooney-Rivlin	C_2	40	[Pa]
Spring stiffness base	k_b	1	[kPa]
Pericardial spring stiffness			
Case *free*	k_p	0	$\left[\frac{\text{kPa}}{\text{mm}}\right]$
Case *pericardium*	k_p	20	$\left[\frac{\text{kPa}}{\text{mm}}\right]$
Case *pseudo-contact*	k_p	20	$\left[\frac{\text{kPa}}{\text{mm}}\right]$

(a) Parameters of the elastodynamical model.

Table 3: Overview of material parameters in ellipsoid model. For numerical parameters see table 1d.

2. Sainte-Marie J, Chapelle D, Cimrman R, Sorine M. Modeling and estimation of the cardiac electromechanical activity. *Computers & Structures.* 2006;84(28):1743–1759.
3. Doost S. N, Ghista D, Su B, Zhong L, Morsi Y. S. Heart blood flow simulation: a perspective review. *BioMedical Engineering OnLine.* 2016;15(1):101.
4. Kerckhoffs R. C, et al. Coupling of a 3D finite element model of cardiac ventricular mechanics to lumped systems models of the systemic and pulmonic circulation. *Annals of Biomedical Engineering.* 2007;35(1):1–18.
5. Holt J. P. The normal pericardium. *The American Journal of Cardiology.* 1970;26(5):455–465.
6. Martini F. H, Timmons M. J, Tallitsch R. B. *Human Anatomy.* Pearson Education; 2015.
7. Standring S. *Gray's Anatomy: The Anatomical Basis of Clinical Practice.* Elsevier Health Sciences; 2015.
8. Lee J. M, Boughner D. R. Mechanical properties of human pericardium. Differences in viscoelastic response when compared with canine pericardium.. *Circulation Research.* 1985;57(3):475–481.
9. Spodick D. H. *The pericardium: a comprehensive textbook.* Informa Health Care; 1996.
10. Rabkin S. W. Epicardial fat: properties, function and relationship to obesity. *Obesity Reviews.* 2007;8(3):253–261.
11. Spodick D. H. The normal and diseased pericardium: Current concepts of pericardial physiology, diagnosis and treatment. *Journal of the American College of Cardiology.* 1983;1(1):240-251.
12. Shabetai R. *The Pericardium.* Springer; 2003.
13. Sacks M. S. Incorporation of experimentally-derived fiber orientation into a structural constitutive model for planar collagenous tissues. *Journal of Biomechanical Engineering.* 2003;125(2):280–287.
14. Glantz S. A, et al. The pericardium substantially affects the left ventricular diastolic pressure-volume relationship in the dog. *Circulation Research.* 1978;42(3):433-41.
15. Hammond H. K, White F. C, Bhargava V, Shabetai R. Heart size and maximal cardiac output are limited by the pericardium. *American Journal of Physiology - Heart and Circulatory Physiology.* 1992;263(6):H1675–H1681.
16. Jöbsis P. D, et al. The visceral pericardium: macromolecular structure and contribution to passive mechanical properties of the left ventricle. *American Jour-*

nal of Physiology - Heart and Circulatory Physiology. 2007;293(6):H3379–H3387.
17. Holt J. P, Rhode E. A, Kines H, Ruth H. Pericardial and Ventricular Pressure. *Circulation Research.* 1960;8(6):1171-1181.
18. Santamore W. P, Constantinescu M. S, Bogen D, Johnston W. E. Nonuniform distribution of normal pericardial fluid. *Basic Research in Cardiology.* 1990;85(6):541–549.
19. Smiseth O. A, Frais M. A, Kingma I, Smith E. R, Tyberg J. V. Assessment of pericardial constraint in dogs. *Circulation.* 1985;71(1):158-64.
20. Tyberg J. V, et al. The relationship between pericardial pressure and right atrial pressure: an intraoperative study. *Circulation.* 1986;73(3):428-32.
21. Hills B. A, Butler B. D. Phospholipids identified on the pericardium and their ability to impart boundary lubrication. *Annals of Biomedical Engineering.* 1985;13(6):573–586.
22. Sudak F. Intrapericardial and intracardiac pressures and the events of the cardiac cycle in Mustelus canis (Mitchill). *Comparative Biochemistry and Physiology.* 1965;14(4):689 - 705.
23. Sutton J, Gibson D. G. Measurement of postoperative pericardial pressure in man. *British Heart Journal.* 1977;39(1):1-6.
24. Mansi T. Image-based physiological and statistical models of the heart: application to tetralogy of Fallot. Phd-thesis, École Nationale Supérieure des Mines de Paris 2010.
25. Chabiniok R, et al. Estimation of tissue contractility from cardiac cine-MRI using a biomechanical heart model. *Biomechanics and Modeling in Mechanobiology.* 2012;11(5):609-630.
26. Marchesseau S, Delingette H, Sermesant M, Ayache N. Fast parameter calibration of a cardiac electromechanical model from medical images based on the unscented transform. *Biomechanics and Modeling in Mechanobiology.* 2013;12(4):815–831.
27. Santiago A, et al. Fully coupled fluid-electro-mechanical model of the human heart for supercomputers. *International Journal for Numerical Methods in Biomedical Engineering.* 2018;.
28. Sermesant M, et al. Patient-specific electromechanical models of the heart for the prediction of pacing acute effects in CRT: A preliminary clinical validation. *Medical Image Analysis.* 2012;16(1):201 - 215.
29. Moireau P, et al. External tissue support and fluid–structure simulation in blood flows. *Biomechanics and Modeling in Mechanobiology.* 2012;11(1-2):1–18.
30. Moireau P, et al. Sequential identification of boundary support parameters in a fluid-structure vascular model using patient image data. *Biomechanics and Modeling in Mechanobiology.* 2013;12(3):475-496.
31. Augustin C. M, et al. Anatomically accurate high resolution modeling of human whole heart electromechanics: A strongly scalable algebraic multigrid solver method for nonlinear deformation. *Journal of Computational Physics.* 2016;305:622 - 646.
32. Land S, Niederer S. A. Influence of atrial contraction dynamics on cardiac function. *International Journal for Numerical Methods in Biomedical Engineering.* 2017;DOI:10.1002/cnm.2931.
33. Baillargeon B, Rebelo N, Fox D. D, Taylor R. L, Kuhl E. The Living Heart Project: A robust and integrative simulator for human heart function. *European Journal of Mechanics - A/Solids.* 2014;48(0):38 - 47.
34. Fritz T, Wieners C, Seemann G, Steen H, Dössel O. Simulation of the contraction of the ventricles in a human heart model including atria and pericardium. *Biomechanics and Modeling in Mechanobiology.* 2013;13(3):1–15.
35. Holzapfel G. A, Ogden R. W. Constitutive modelling of passive myocardium: a structurally based framework for material characterization. *Philosophical Transactions of the Royal Society A: Mathematical, Physical and Engineering Sciences.* 2009;367(1902):3445–3475.
36. Rabkin S, Hsu P. Mathematical and mechanical modeling of stress-strain relationship of pericardium. *American Journal of Physiology – Legacy Content.* 1975;229(4):896–900.
37. Hirschvogel M, Bassilious M, Jagschies L, Wildhirt S, Gee M. A monolithic 3D-0D coupled closed-loop model of the heart and the vascular system: Experiment-based parameter estimation for patient-specific cardiac mechanics. *International Journal for Numerical Methods in Biomedical Engineering.* 2016;33(8):e2842.
38. Uribe S, et al. Volumetric Cardiac Quantification by Using 3D Dual-Phase Whole-Heart MR Imaging. *Radiology.* 2008;248(2):606–614.
39. Geuzaine C, Remacle J.-F. Gmsh: A 3-D finite element mesh generator with built-in pre-and post-processing facilities. *International Journal for Numerical Methods in Engineering.* 2009;79(11):1309–1331.
40. Nagler A, Bertoglio C, Ortiz M, Wall W. A. *A spatially varying mathematical representation of the biventricular cardiac fiber architecture.* technical report: Institute for Computational Mechanics, Technische Universität München ; Center for Mathematical Modeling, Universidad de Chile ; 2016.
41. Ubbink S, Bovendeerd P, Delhaas T, Arts T, Vosse F. Towards model-based analysis of cardiac MR tagging data: Relation between left ventricular shear strain and myofiber orientation. *Medical Image Analysis.* 2006;10(4):632 - 641. Special Issue on Functional Imaging and Modelling of the Heart (FIMH 2005).
42. Wong K. C. L, et al. Cardiac Motion Estimation Using a ProActive Deformable Model: Evaluation and Sensitivity Analysis. In: Springer Berlin Heidelberg; 2010; Berlin, Heidelberg.
43. Gil D, et al. What a Difference in Biomechanics Cardiac Fiber Makes. In: Camara O, Mansi T, Pop M, Rhode K, Sermesant M, Young A, eds. *Statistical Atlases and Computational Models of the Heart. Imaging and Modelling Challenges*, Lecture Notes in Computer Science, vol. 7746: Springer Berlin Heidelberg 2013 (pp. 253-260).
44. Eriksson T, Prassl A, Plank G, Holzapfel G. Influence of myocardial fiber/sheet orientations on left ventricular mechanical contraction. *Mathematics and Mechanics of Solids.* 2013;18(6):592-606.
45. Asner L, et al. Estimation of passive and active properties in the human heart using 3D tagged MRI. *Biomechanics and Modeling in Mechanobiology.* 2016;15(5):1121–1139.
46. Nikou A, Gorman R. C, Wenk J. F. Sensitivity of left ventricular mechanics to myofiber architecture: A finite element study. *Proceedings of the Institution of Mechanical Engineers, Part H: Journal of Engineering in Medicine.* 2016;230(6):594-598. PMID: 26975892.
47. Hörmann J. M, et al. Multiphysics Modeling of the Atrial Systole under Standard Ablation Strategies. *Cardiovascular Engineering and Technology.* 2017;8(2):205–218.
48. Hörmann J. M, Pfaller M. R, Bertoglio C, Avena L, Wall W. A. Automatic Mapping of Atrial Fiber Orientations

for Patient-Specific Modeling of Cardiac Electromechanics using Image-Registration. *submitted to International Journal for Numerical Methods in Biomedical Engineering.* 2018;.
49. Chapelle D, Le Tallec P, Moireau P, Sorine M. An energy-preserving muscle tissue model: formulation and compatible discretizations. *International Journal for Multiscale Computational Engineering.* 2012;10(2):189–211.
50. Bestel J, Clément F, Sorine M. A Biomechanical Model of Muscle Contraction. In: Niessen W. J, Viergever M. A, eds. *Medical Image Computing and Computer-Assisted Intervention – MICCAI 2001*, Springer Berlin Heidelberg; 2001; Berlin, Heidelberg.
51. Hörmann J. M, et al. An adaptive Hybridizable Discontinuous Galerkin approach for cardiac electrophysiology. *International Journal for Numerical Methods in Biomedical Engineering.* 2018;34(5):e2959.
52. Newmark N. M. A method of computation for structural dynamics. *Journal of the Engineering Mechanics Division.* 1959;85(3):67–94.
53. Chung J, Hulbert G. A time integration algorithm for structural dynamics with improved numerical dissipation: the generalized-α method. *Journal of Applied Mechanics.* 1993;60(2):371–375.
54. Westerhof N, Lankhaar J.-W, Westerhof B. E. The arterial windkessel. *Medical & Biological Engineering & Computing.* 2008;47(2):131–141.
55. Shi Y, Lawford P, Hose R. Review of zero-D and 1-D models of blood flow in the cardiovascular system. *Biomed Eng Online.* 2011;10:33.
56. Gee M. W, Reeps C, Eckstein H. H, Wall W. A. Prestressing in finite deformation abdominal aortic aneurysm simulation. *Journal of Biomechanics.* 2009;42(11):1732 - 1739.
57. Gee M. W, Förster C, Wall W. A. A computational strategy for prestressing patient-specific biomechanical problems under finite deformation. *International Journal for Numerical Methods in Biomedical Engineering.* 2010;26(1):52–72.
58. Wall W. A, et al . *Baci: a parallel multiphysics simulation environment.* : Technical report, Institute for Computational Mechanics, Technische Universität München; 2018.
59. Carlsson M, Ugander M, Mosén H, Buhre T, Arheden H. Atrioventricular plane displacement is the major contributor to left ventricular pumping in healthy adults, athletes, and patients with dilated cardiomyopathy. *American Journal of Physiology - Heart and Circulatory Physiology.* 2007;292(3):H1452–H1459.
60. Willenheimer R, Cline C, Erhardt L, Israelsson B. Left ventricular atrioventricular plane displacement: an echocardiographic technique for rapid assessment of prognosis in heart failure. *Heart.* 1997;78(3):230–236.
61. Heiberg E, et al. Design and validation of Segment - freely available software for cardiovascular image analysis. *BMC Medical Imaging.* 2010;10(1):1.
62. Lee L. C, Sundnes J, Genet M, Wenk J. F, Wall S. T. An integrated electromechanical-growth heart model for simulating cardiac therapies. *Biomechanics and Modeling in Mechanobiology.* 2016;15(4):791–803.
63. Arutunyan A. H. Atrioventricular plane displacement is the sole mechanism of atrial and ventricular refill. *American Journal of Physiology-Heart and Circulatory Physiology.* 2015;308(11):H1317-H1320. PMID: 25795710.
64. Arvidsson P. M, Carlsson M, Kovács S. J, Arheden H. Letter to the Editor: Atrioventricular plane displacement is not the sole mechanism of atrial and ventricular refill. *American Journal of Physiology-Heart and Circulatory Physiology.* 2015;309(6):H1094-H1096. PMID: 26374902.
65. Maksuti E, Bjällmark A, Broomé M. Modelling the heart with the atrioventricular plane as a piston unit. *Medical Engineering & Physics.* 2015;37(1):87 - 92.
66. Fujii K, et al. Effect of left ventricular contractile performance on passive left atrial filling - Clinical study using radionuclide angiography. *Clinical Cardiology.* 1994;17(5):258–262.
67. Emilsson K, Brudin L, Wandt B. The mode of left ventricular pumping: is there an outer contour change in addition to the atrioventricular plane displacement?. *Clinical Physiology.* 2001;21(4):437-446.
68. Bowman A. W, Kovács S. J. Assessment and consequences of the constant-volume attribute of the four-chambered heart. *American Journal of Physiology-Heart and Circulatory Physiology.* 2003;285(5):H2027-H2033. PMID: 12869381.
69. Yin F. C, Strumpf R. K, Chew P. H, Zeger S. L. Quantification of the mechanical properties of noncontracting canine myocardium under simultaneous biaxial loading. *Journal of Biomechanics.* 1987;20(6):577 - 589.
70. Dokos S, Smaill B. H, Young A. A, LeGrice I. J. Shear properties of passive ventricular myocardium. *American Journal of Physiology - Heart and Circulatory Physiology.* 2002;283(6):H2650–H2659.
71. Sommer G, et al. Biomechanical properties and microstructure of human ventricular myocardium. *Acta Biomaterialia.* 2015;24:172–192.
72. Gültekin O, Sommer G, Holzapfel G. A. An orthotropic viscoelastic model for the passive myocardium: continuum basis and numerical treatment. *Computer Methods in Biomechanics and Biomedical Engineering.* 2016;0(0):1-18. PMID: 27146848.
73. Nagler A, Bertoglio C, Stoeck C. T, Kozerke S, Wall W. A. Maximum likelihood estimation of cardiac fiber bundle orientation from arbitrarily spaced diffusion weighted images. *Medical Image Analysis.* 2017;39:56 - 77.